Automated identification, industrial attribution and conditional emission-rate quantification of recurrent CO enhancement source regions from TROPOMI observations

Authors

Haoyi Wu[1,*]; Renwei Meng[1]

Affiliation

[1]Stony Brook Institute at Anhui University, No. 3 Feixi Road, Shushan District, Hefei, Anhui 230039, China

Correspondence

Haoyi Wu - r32314010@stu.ahu.edu.cn - ORCID: https://orcid.org/0009-0007-5022-4925

Co-author

Renwei Meng - r32314095@stu.ahu.edu.cn - ORCID: https://orcid.org/0009-0001-6879-6629

Automated identification, industrial attribution and conditional emission-rate quantification of recurrent CO enhancement source regions from TROPOMI observations

Haoyi Wu[a,1,*], Renwei Meng[a,2]

[a]*Stony Brook Institute at Anhui University, No. 3 Feixi Road, Shushan District, Hefei, Anhui 230039, China*

Abstract

The TROPOspheric Monitoring Instrument (TROPOMI) repeatedly measures global carbon monoxide (CO) total columns, but industrial CO studies generally begin with known cities or facilities; a general method is therefore needed to discover where enhancements recur globally. We developed an automated workflow that searches without facility coordinates. A weakly supervised model screens scenes for localized CO enhancements; corrected CO pixels then delineate their footprints, duplicate detections within an overpass are merged, and nearby enhancements on different dates are grouped into candidate source regions. Only afterward are industrial facilities and active fires introduced to assess industrial context. Polygon-CSF estimates instantaneous emission rates only when enhancement geometry and winds permit cross-sectional calculation. Applied to 20,279 TROPOMI Level-2 CO product files from 2020 to 2023, the workflow identified 25,587 independent enhancement observations and 13,363 candidate source regions. Of these, 4,986 were observed at least twice and 168 at least 10 times; 134 of the latter were detected in all four years. The proportion with a nearby industrial facility record rose from 38.1% among single-observation regions to 81.0% among regions observed at least 10 times. Among 180 regions with the strongest industrial evidence, 136 contained multiple industrial facility types. Under qualifying conditions, polygon-CSF yielded 512 instantaneous emission-rate estimates across 177 regions, with a region-level median of 35.0 Mg h^{-1}. By linking automated global CO-enhancement discovery, industrial attribution and conditional emission-rate quantification, the workflow prioritizes industrial areas for verification and continued monitoring.

Keywords:
carbon monoxide, TROPOMI, automated detection, recurrent observations, industrial source regions, cross-sectional flux method, instantaneous emission rate

1. Introduction

Carbon monoxide (CO) is produced primarily by incomplete combustion. It is an important air pollutant and a tracer of combustion emissions and atmospheric transport. Large iron and steel, coal-conversion, thermal-power and metallurgical activities can produce localized CO enhancements detectable from space [7, 12, 16]. TROPOMI provides continuing near-global CO

*Corresponding author
Email addresses: r32314010@stu.ahu.edu.cn (Haoyi Wu), r32314095@stu.ahu.edu.cn (Renwei Meng)
[1]ORCID: 0009-0007-5022-4925
[2]ORCID: 0009-0001-6879-6629

total-column observations [1–5, 15], so recurrence at the same location on different dates can be used to screen a global archive for locations requiring further investigation.

Most previous TROPOMI CO studies have focused on known cities, fires, or industrial facilities [6–9, 12, 16]. Investigators generally specify a target first, then define the background, match the wind field and estimate emissions. These studies establish what TROPOMI can measure for large CO sources, but they do not provide a systematic way to discover unknown locations that recur in global observations. The required transition is therefore to build a traceable source-region catalogue from the satellite observations first, and only then interpret the catalogue and quantify emission rates.

Finding such locations automatically requires three linked operations. Four years of data contain tens of thousands of Level-2 products, each of which can be divided into many overlapping local scenes; manual inspection would be slow and difficult to standardize. Regional gradients, long-range transport, missing-data boundaries and residual striping can resemble locally emitted enhancements [5, 15]. Overlapping scenes can also record the same signal more than once during one overpass. An automated workflow must therefore screen candidate scenes, delineate the enhancement from CO pixels, and consolidate duplicate detections into one observation per overpass.

Schuit et al. [10] used a convolutional neural network and a support vector classifier to identify methane plumes automatically in TROPOMI observations and locate persistent emission regions. Their study showed that large-scale automated screening can be linked to subsequent source analysis. The CO training data available for the present study provide only a label indicating whether an entire scene contains an enhancement; they do not identify the pixels occupied by that enhancement [11, 21]. This training setting, in which image-level classes are available but object locations are not, is known as weakly supervised learning [17–20]. It can indicate that an enhancement may be present in a scene, but it cannot determine where the enhancement lies or which pixels it covers. The corrected CO total-column field must therefore be analysed after model screening to delineate each enhancement. This footprint is required to determine whether enhancements on different dates occurred in the same area, to measure their proximity to industrial facilities, and to estimate emission rates.

Source assessment remains constrained by TROPOMI's spatial resolution even after an enhancement footprint has been delineated. Large industrial complexes often contain several neighbouring facilities and production processes; a single CO enhancement may cover adjacent steelmaking, coking, and power-generation units. Assigning the nearest plant as the sole source can therefore omit other industrial activities within the observed enhancement. We instead use the distribution of facilities, their sectoral composition, and same-day active-fire detections to assess likely sources at the scale of the industrial area. This interpretation better matches the spatial information that TROPOMI can resolve.

Emission-rate estimation addresses a separate question. Previous studies have shown that cross-sectional flux methods can estimate CO emissions from industrial sources and cities observed by TROPOMI [7, 9, 12, 16]. These calculations require enhancement geometry and wind fields that are suitable for cross-sectional analysis. Even when those requirements are met, an individual overpass yields an emission magnitude at the satellite overpass time rather than a long-term mean emission rate. We therefore distinguish how often an enhancement is detected at a location from the instantaneous emission rate estimated during qualifying overpasses. The former describes whether an observable enhancement recurs; the latter describes its magnitude during a particular observation.

Here we develop an automated workflow for global TROPOMI CO observations from 2020-

2023. Facility coordinates are not used during the search. A model first screens scenes that may contain localized enhancements. The enhancement footprints are then delineated from the corrected CO total-column field, and duplicate detections from the same overpass are merged. Enhancements observed on different dates at nearby locations are subsequently grouped into candidate source regions. Only after these regions have been established are facility and active-fire data used to assess possible industrial sources; instantaneous emission rates are then estimated for overpasses that meet the required image and wind conditions. We examine the recurrence of the resulting regions over four years, their spatial relationships with industrial facilities, and the distribution of their instantaneous emission rates. Six industrial-area case studies further show how the satellite enhancements correspond to facilities on the ground.

2. Data and methods

Figure 1 summarizes the complete workflow. TROPOMI observations are first divided into 32×32-pixel scenes. PG37-MIL, a multiple-instance learning model using 37 proposal-region features, screens the scenes for possible localized CO enhancements. The workflow then returns to the corrected CO pixels to delineate each enhancement footprint. CEQ-36, a 36-feature CO enhancement-quality model, evaluates whether the delineated enhancement is sufficiently coherent for the subsequent analysis. Duplicate detections from one overpass are merged, and enhancements observed on different dates at nearby locations are grouped into candidate source regions. Industrial facilities, active fires and wind fields are introduced only after this discovery sequence, to assess the industrial context and estimate conditional instantaneous emission rates. Facility coordinates do not enter the global search. The upper part of Fig. 1 follows one observed overpass through the complete sequence; the lower part summarizes its three main stages.

2.1. TROPOMI and auxiliary data

We analysed 20,279 TROPOMI Level-2 CO product files acquired from 2020 to 2023. The initial search used the officially corrected CO total column, quality flags, and pixel-centre and corner coordinates supplied with each product. Only finite pixels with `qa_value` ≥ 0.5 were retained [5]. The search covered land and near-coastal areas between 65° S and 65° N. To retain industrial areas close to coastlines, the land test also examined locations within 0.15° of each candidate; detections entirely over the open ocean were excluded. Annual file counts and the complete screening criteria are provided in Supplementary Section S1.

Auxiliary data comprised wind fields from the European Centre for Medium-Range Weather Forecasts Reanalysis v5 (ERA5) [14], active-fire detections from the Visible Infrared Imaging Radiometer Suite (VIIRS) aboard Suomi NPP and NOAA-20 [13], and catalogues of energy and heavy-industrial facilities. ERA5 supplied the mean wind speed and direction at 150–250 m for the satellite overpass time. The two VIIRS products were used to check for active fires on the same UTC date, and facility catalogues described the industrial activities near each enhancement. All auxiliary data were introduced only after a CO enhancement had been detected.

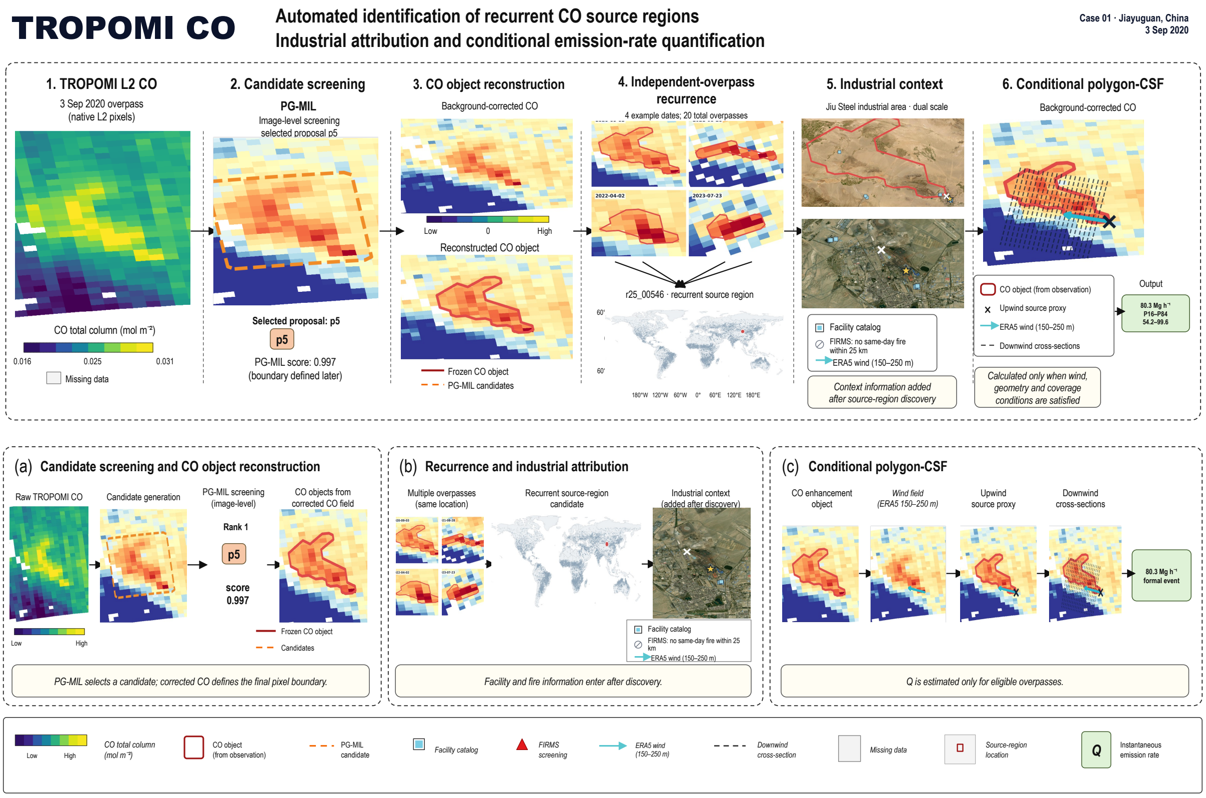

Figure 1: From a single TROPOMI observation to recurrent industrial CO source regions and conditional emission rates. The upper part uses an actual 3 September 2020 overpass over the Jiugang industrial area to show the TROPOMI Level-2 CO product, PG37-MIL candidate screening, the enhancement extent redefined from corrected CO pixels, repeated observations at the same location on multiple dates, the industrial facilities and active-fire context added after the search, and polygon-CSF calculation when the conditions are met. The lower part summarizes three key stages: PG37-MIL ranks candidate regions only, while the final enhancement boundary is determined from the corrected CO field (a); after enhancements from different overpasses are grouped into recurrent source regions, facilities, same-day fires and ERA5 winds are added to interpret the industrial context (b); instantaneous emission rates are estimated only for overpasses that meet the image, coverage and wind requirements (c). PG-MIL in the figure is an abbreviation for PG37-MIL. The formal emission rate for this overpass is 80.3 Mg h−1; Fig. 8 shows another overpass of the same source region on 28 August 2021, so the emission rates in the two figures differ. Basemap imagery is from Esri World Imagery; source credits are provided by Esri, Maxar, Earthstar Geographics, and the GIS User Community. OpenAI ChatGPT and Codex assisted with the explanatory layout; the underlying satellite observations, quantitative results and analyses were not generated or altered by these tools.

2.2. Scene screening with PG37-MIL

The model was trained with the AutoMerge CO dataset [11, 21]. Each 32 × 32-pixel scene carries one label indicating whether an enhancement is present, but no annotation marks the pixels occupied by that enhancement. This is a weakly supervised learning setting [17–20]. To learn localized information from scene-level labels, we first generated several possible high-value regions within each scene and applied the same scoring network to each region. At least one region in a positive scene should receive a high score, whereas all regions in a negative scene should receive low scores. The model therefore learns which local structures best explain the label of the complete scene.

We refer to the model as PG37-MIL, short for proposal-guided multiple-instance learning with 37 proposal features. Here, multiple-instance learning means that one scene contains several proposal regions to be evaluated, while the training label applies only to the complete scene. The model scores each proposal separately and combines the scores into a scene-level score. Its role is to identify locations that warrant further examination, not to delineate the final enhancement boundary.

Proposal generation was deliberately permissive so that the first stage would be less likely to miss a genuine enhancement. The scene median was used as the local background, and each pixel's CO excess relative to that background was converted to a dimensionless robust standardized score, z. A larger z indicates a stronger positive departure from the local background. Pixels with $z \geq 2.0$ initiated high-value cores, which were expanded through connected pixels with $z \geq 1.0$. Each proposal contained at least three pixels, including at least one core pixel. The valid-pixel fraction had to reach 0.80 in the broad background area, 0.80 in the complete scene and 0.85 around the proposal, preventing decisions based mainly on missing data. The complete formula, missing-data treatment and comparisons with neighbouring parameter values are given in Supplementary Section S2.

Each proposal was represented by 37 features describing CO enhancement strength and shape, retrieval quality, missing data, and position within the scene and satellite swath. Wind, facility and fire information, year and subsequent recurrence were excluded. The scoring network had a 37–32–16–1 architecture: the 37 features passed through hidden layers of 32 and 16 neurons to produce a proposal score (Fig. 3). Proposal scores within a scene were combined with a proposal-count-corrected log-sum-exp function. This function acts as a smooth maximum: it is driven mainly by the highest-scoring proposal, while preventing a scene with more proposals from receiving a higher score simply because it contains more proposals.

The dataset was divided into fixed sets of 3,319 training scenes, 830 validation scenes and 1,058 test scenes. The model architecture and operating threshold were selected using only the training and validation sets; the test set was not used for either choice. The global search used the validation-derived threshold of 0.283247.

On the independent test set, precision was 0.838: 83.8% of the scenes selected by the model agreed with the manual labels. Recall was 0.825: 82.5% of the scenes labelled as containing an enhancement were identified. The harmonic mean of precision and recall, the F1 score, was 0.831. The area under the precision–recall curve, PR-AUC, was 0.8835. For each scene above the threshold, only the highest-scoring proposal that met the quality requirements was passed to the next stage, where the footprint was determined anew. Figure 2 distinguishes a proposal region from the final enhancement footprint, and Fig. 3 shows the model architecture. The 37 features and training configuration are reported in Supplementary Sections S7–S8.

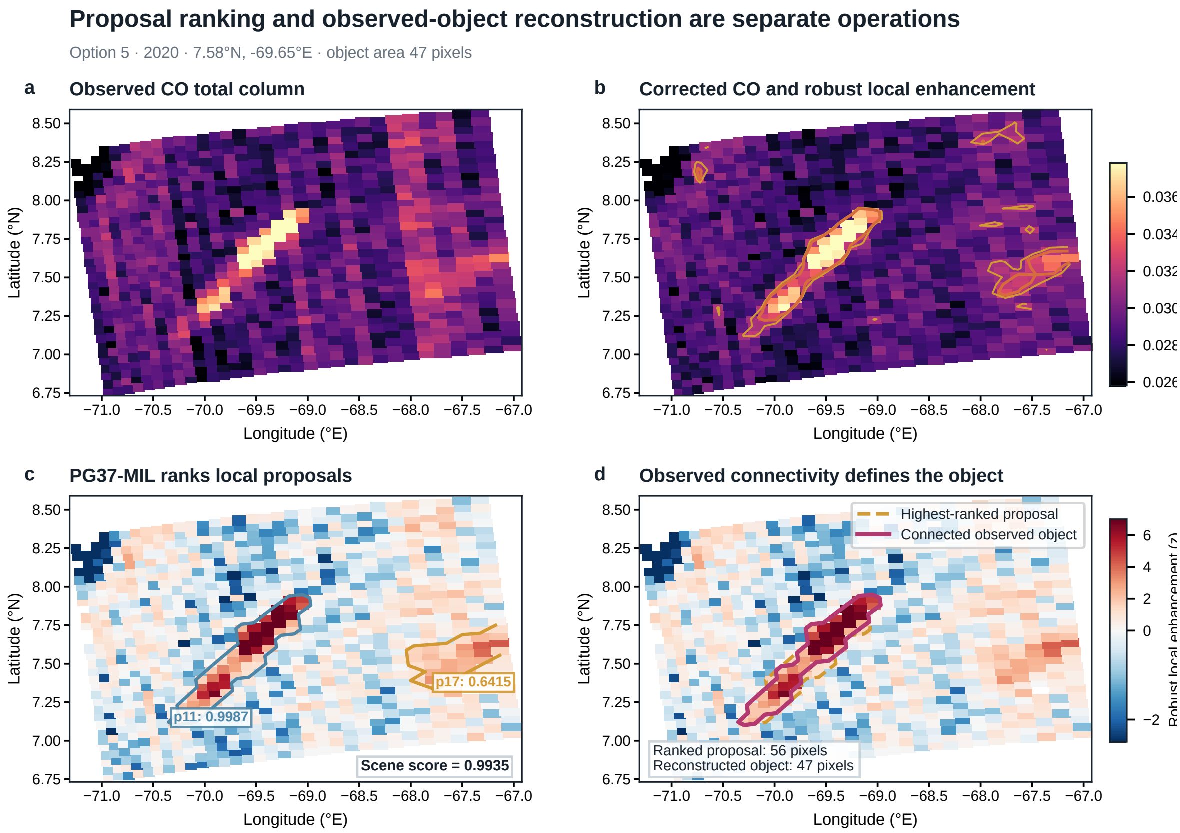

Figure 2: The model indicates a possible location, and the enhancement extent is redefined from CO pixels. The example is the 2 January 2020 overpass near 7.58°N, 69.65°W. The original CO total column is shown in (a), and the corrected CO field with local enhancement contours is shown in (b). PG37-MIL scores two candidate regions separately, and the candidate scores are used to obtain the score for the complete scene (c). The highest-scoring candidate contains 56 pixels, with a score of 0.9987, whereas the connected enhancement object reconstructed from corrected CO contains 47 pixels (d). The second candidate has a score of 0.6415 and the scene score is 0.9935. Model scores rank candidate regions and do not represent the probability that a pixel belongs to an enhancement; the reconstructed object is used for subsequent facility-distance and emission-rate calculations.

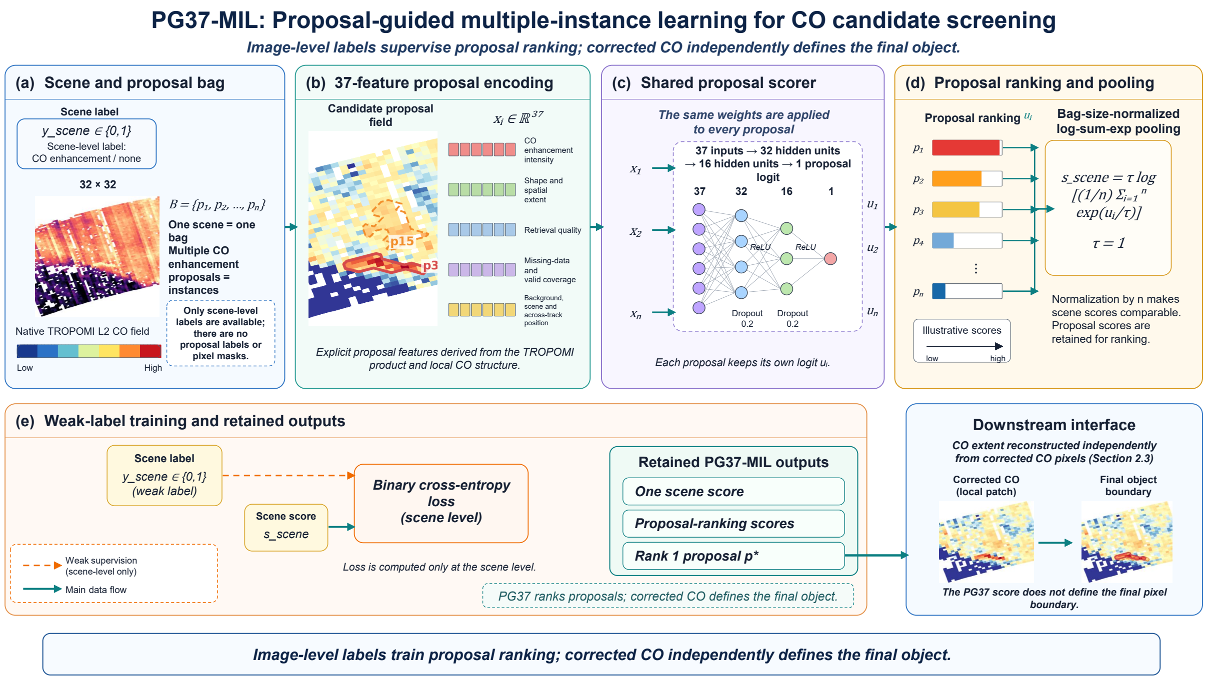

Figure 3: How PG37-MIL converts a scene label into a ranking of candidate regions. A 32 × 32-pixel scene is treated as a bag containing multiple candidate regions as instances to be scored; the training data provide only a label indicating whether the complete scene contains an enhancement, not candidate labels or a pixel mask (a). Each candidate is described by 37 features of CO intensity, shape and spatial extent, retrieval quality, missingness and valid coverage, and its position relative to the background and satellite swath (b). A shared 37–32–16–1 feed-forward network uses the same weights to calculate each candidate score (c). A candidate-count-corrected log-sum-exp function with temperature $\tau = 1$ then aggregates the candidate scores into a scene score while retaining the candidate ranking (d). The loss is calculated only from the scene label; retained outputs include the scene score, candidate scores and the top-ranked candidate region (e). PG37-MIL does not generate a pixel mask; the final enhancement boundary is independently determined from corrected CO pixels in the next step. OpenAI ChatGPT and Codex assisted with the explanatory layout; all architecture labels and numerical content were supplied and verified by the authors.

2.3. Delineating CO enhancement footprints

The PG37-MIL proposal indicates only the approximate location of a local high-value feature. Because proposals are generated with permissive criteria, their boundaries are not used directly for facility distances or emission rates. Instead, the corrected CO total-column field is reanalysed across the complete scene, and the pixels occupied by the enhancement are delineated from their connectivity (Fig. 2).

Starting from the valid pixel with the highest standardized score within the proposal, the algorithm expands in all eight neighbouring directions across the complete 32×32-pixel scene. Connected pixels with $z \geq 1.7$ can enter the enhancement footprint, provided that the resulting region contains at least one high-value core pixel with $z \geq 2.4$ within the original proposal extent. The lower threshold retains weaker pixels connected to the core, while the higher threshold ensures that the footprint contains a distinct enhancement. Missing pixels cannot connect otherwise separate regions.

For every delineated enhancement, we store the included pixels, their centres and all four corners of each pixel. This same footprint is used for facility-distance and cross-sectional-flux calculations, so source assessment and emission-rate estimation refer to one identical set of CO pixels. Comparisons of the two thresholds with neighbouring alternatives are provided in Supplementary Section S8.1.

2.4. Enhancement-quality scoring with CEQ-36

Connectivity alone does not ensure that an enhancement is suitable for further analysis. Some detections contain only one isolated high value, some are truncated by missing data, and others lie within broad concentration gradients or fields containing several mixed high-value features. CEQ-36 therefore scores each delineated enhancement. PG37-MIL searches many scenes for possible enhancements; CEQ-36 then evaluates whether the enhancement is spatially coherent and whether its surroundings provide a sufficiently clear background for the subsequent analysis.

An expert first assigned examples to four ordered classes according to enhancement continuity and background clarity; indeterminate examples were excluded from training. The final training set contained 587 enhancements from 2023. CEQ-36 is an ExtraTrees model whose ensemble of randomized decision trees produces a continuous quality score, S_{CEQ}. Higher scores indicate more coherent enhancements with clearer surrounding backgrounds. Its 36 inputs describe core strength, enhancement-to-background contrast, pixel connectivity and fragmentation, broader background variation, missing data and retrieval quality. Facility and fire information, recurrence and emission rate are not used in the score.

To test whether the score remained informative outside its training year, we independently selected 90 enhancements not used for training, with 30 from each year between 2020 and 2022. Model scores increased with expert-assigned quality (Spearman rank correlation $\rho = 0.814$). After the four classes were combined into higher- and lower-quality groups, the area under the receiver operating characteristic curve was 0.955. CEQ-36 therefore remained consistent with expert assessments in other years. Subsequent analyses retained enhancements with $S_{\mathrm{CEQ}} \geq 1.50$. The complete class definitions, training and validation procedures, threshold selection and 36 inputs are given in Supplementary Sections S7.2 and S8.3. These module-specific checks are summarized in Fig. 4.

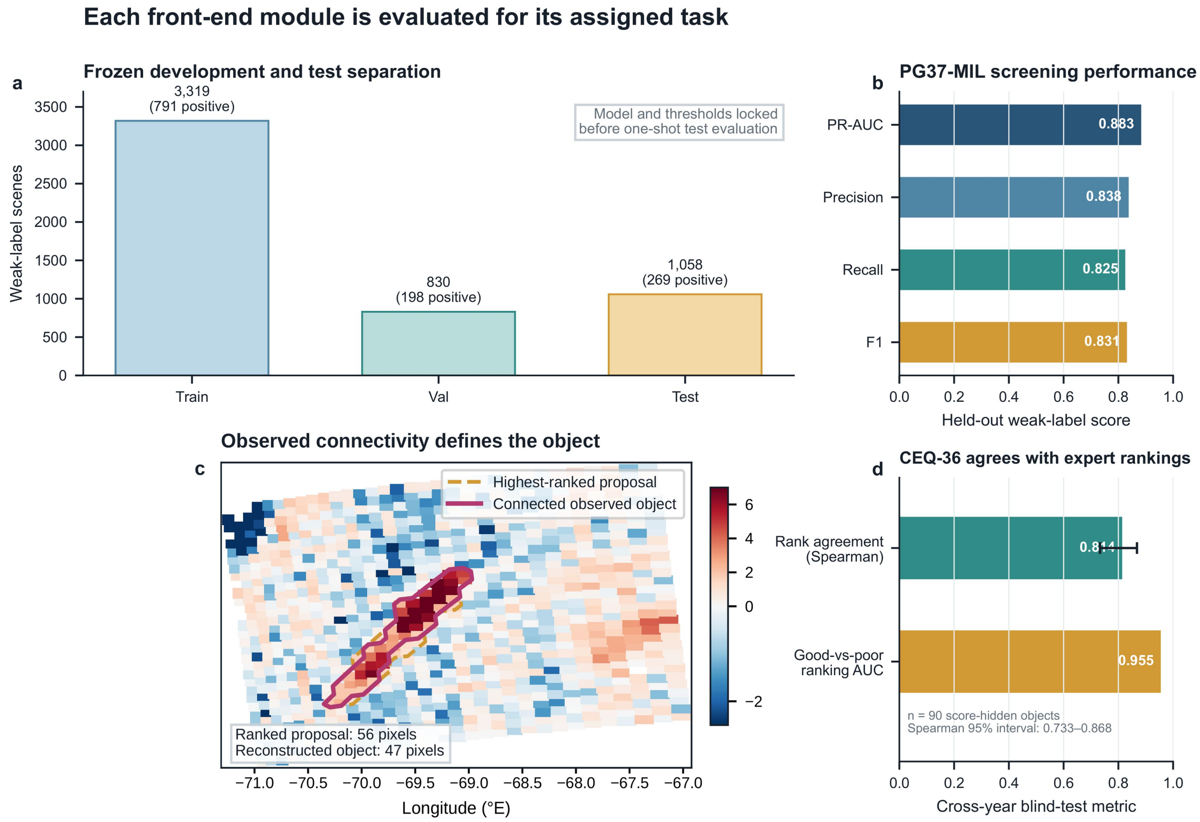

Figure 4: Separate evaluation of scene screening, enhancement-extent determination and quality scoring. The fixed data split contains 3,319 training scenes, 830 validation scenes and 1,058 test scenes; the model structure and operating threshold were determined before test-set evaluation (a). On the independent test set, the area under the precision–recall curve (PR-AUC) of PG37-MIL was 0.8835; at the validation-set threshold, precision, recall and their harmonic mean, F1, were 0.838, 0.825 and 0.831, respectively (b). Panel (c) uses the same 2 January 2020 example as Fig. 2 to illustrate that corrected-CO connectivity reconstructs the observed object separately from the highest-ranked proposal: 56 proposal pixels are reduced to a 47-pixel connected object. Across all 25,587 independent enhancement observations, the reconstructed footprint area has a median of 17 pixels. The quality ranking assigned by CEQ-36 to 90 samples from 2020–2022 that did not participate in training agreed well with expert judgement, with a Spearman correlation of 0.814 and a 95% interval of 0.733–0.868; the area under the receiver operating characteristic curve (AUC) for distinguishing better from poorer enhancements was 0.955 (d). The three groups of results evaluate, in order, whether the model can screen scenes, whether enhancement extents can be determined from CO pixels, and whether the quality score can be used for other years.

2.5. *Recurrent source regions, industrial-source assessment, and emission rates*

2.5.1. *Merging duplicate detections and establishing source regions*

Overlapping scenes can cover the same enhancement repeatedly and can therefore produce several records from one satellite overpass. Records with the same observation start time and orbit number were first merged, retaining only the record with the highest quality score. Each resulting record represents one enhancement observed during one satellite overpass and is hereafter termed an independent enhancement observation.

Independent observations from different dates were then compared. The highest-quality observation not yet assigned to a region established the source-region centre. Other observations were assigned to that region only when they fell within 25 km of the centre, which remained fixed after it was established. Fixing the centre prevents a chain of locally adjacent observations with distant endpoints from being joined into one region. A region's recurrence count is the number of independent enhancement observations assigned to it. Comparisons of the 25-km radius, processing order and boundary conditions are presented in Supplementary Sections S4 and S8.4.

Because the number of valid TROPOMI overpasses differs among locations, recurrence counts alone may reflect differences in satellite sampling. We therefore evaluated every source region against all 20,279 product files and counted the overpasses for which the location had sufficient valid pixels and an estimable background. Detection frequency was defined as the number of enhancement observations divided by the number of valid overpasses. It is the proportion of overpasses with basic observing conditions in which an enhancement was detected again. Complete coverage criteria and comparisons using more permissive and more restrictive definitions are given in Supplementary Section S10.

2.5.2. *Assessing possible industrial sources*

Industrial-facility and active-fire information was introduced only after the source regions had been established. The combined facility database contained 103,608 records from global energy, steel, coal, cement and metallurgical catalogues, together with facility-level CO inventories from several countries. For each enhancement observation, facility distance was measured from a facility coordinate to the nearest pixel centre in the enhancement footprint. The principal search radius was 25 km.

Enhancements near facilities were compared with detections from both VIIRS products on the same Coordinated Universal Time (UTC) date. Absence of a matched fire was recorded only when both VIIRS products completely covered the surrounding 25-km area. The 180 regions used for industrial-composition and emission-rate analyses each had at least five enhancement observations that simultaneously met three criteria: a facility within 25 km, complete same-day fire coverage and no matched active-fire detection. Comparisons using 10- and 50-km search radii are provided in Supplementary Section S5.

To determine whether recurrent enhancements were increasingly concentrated in industrial areas, we divided all 13,363 regions into four groups: observed once, observed 2–4 times, observed 5–9 times, or observed at least 10 times. We compared the proportion of regions near facilities among these groups. For the 5,701 regions with at least one facility record within 25 km, we also compared facility counts and distance to the nearest facility.

Both valid satellite coverage and facility-catalogue density vary geographically. We therefore used regression models to evaluate the relationships of recurrence count with nearby facility count and nearest-facility distance while accounting for valid observing opportunities, geographic location, local facility-record density and enhancement quality. Model variables, facility deduplication and the repeated analysis restricted to Global Energy Monitor records are detailed in Supplementary Section S5.

A TROPOMI enhancement may cover several facilities in one industrial area. We therefore did not designate the nearest facility record as the sole source; instead, we summarized all industrial sectors recorded within 25 km of each region. A region was classified as single-sector dominated only when one sector clearly prevailed. It was classified as multi-sector when several sectors were well represented. Where the catalogues established an industrial presence but did not support a dominant-sector assignment, the sectoral composition was recorded as unknown. Distance weights and classification thresholds are provided in Supplementary Section S5.

Finally, we compared the source-region catalogue with six industrial CO areas reported in previous satellite studies. The purpose was to assess whether the automated search could rediscover known locations. None of the six locations was used for model training, proposal generation or threshold selection.

2.5.3. Estimating instantaneous emission rates

For overpasses with distinct enhancements and suitable winds, we estimated instantaneous emission rates using the cross-sectional flux method [7, 9, 12, 16]. Pixel geometry was represented by the actual corner polygons, so we call this implementation the polygon-based cross-sectional flux method, or polygon-CSF. Several transects perpendicular to the wind direction were placed downwind of the enhancement. The background-subtracted CO column along each transect was integrated and multiplied by wind speed. Actual pixel boundaries allow the true intersection length to be calculated when a transect crosses irregular TROPOMI pixels.

Pixel corners were first projected into a local equidistant coordinate system centred on the enhancement. Transects were then placed downwind from the most upwind enhancement boundary. The background was the median CO column from at least five valid pixels within a 0.30° × 0.30° upwind area. The emission rate from transect j was

$$Q_j = U M_{\mathrm{CO}} \int_{L_j} (\Omega_{\mathrm{CO}} - \Omega_{\mathrm{bg}})\, \mathrm{d}l. \tag{1}$$

Here, U is the ERA5 mean wind speed at 150–250 m, M_CO is the molar mass of CO, $\Omega_{\mathrm{CO}} - \Omega_{\mathrm{bg}}$ is the background-subtracted CO column enhancement, and dl is the length of the intersection between the transect and a pixel polygon. Each overpass produces several transect estimates; their median is used as the overpass estimate so that no single transect determines the result.

The calculation required a wind speed of at least 1.5 m s^{-1}, at least 70% valid-pixel coverage on each transect and at least three valid transect results among a maximum of 20 transects. The wind field was matched to the ERA5 hour nearest to the satellite overpass time. Complete calculation criteria and uncertainty propagation are described in Supplementary Section S6, and parameter-sensitivity comparisons are reported in Section S9.

We also evaluated whether the enhancement elongation was broadly aligned with the wind direction. Schuit et al. [10] used this relationship in methane-plume detection. Here, weighted principal component analysis (PCA) identified the direction along which the enhancement pixels were most extended. Each pixel was weighted by its positive CO excess, so stronger parts of the enhancement contributed more to the orientation estimate. The direction of maximum spatial variance defined the principal axis and was calculated solely from the CO image, without using wind information. Because a principal axis is an undirected line, we used the smaller angle from 0° to 90° between this axis and the ERA5 wind vector, as defined in Eq. (2).

$$\theta = \arccos\left(\frac{|\mathbf{e}_1 \cdot \mathbf{u}|}{\|\mathbf{e}_1\|\,\|\mathbf{u}\|}\right), \qquad 0^\circ \le \theta \le 90^\circ. \tag{2}$$

Here, e_1 is the enhancement principal axis and u is the ERA5 wind vector. Only overpasses with $\theta \le 60^\circ$ and a successful polygon-CSF calculation entered the emission-rate summary. This gate determines whether an already calculated estimate is included; it does not change the estimate itself. At most three overpasses were retained per region, ranked by the number of valid transects, transect coverage, consistency among transect estimates and the number of available background pixels. Emission magnitude did not enter this ranking.

We performed a one-factor-at-a-time sensitivity analysis. In each comparison, one parameter was changed while all others were held constant to assess sensitivity to choices involving the wind field, background, transects, and enhancement boundary. Full results are given in Supplementary Section S9.

Finally, we tested whether regions with more recurrent enhancements also had higher instantaneous emission rates. We first calculated the median of all retained overpass estimates for each source region. Spearman rank correlation then tested whether recurrence count and emission rate had similar rank order, without assuming a linear relationship. To account for differences in satellite observing opportunities, the analysis was repeated with detection frequency in place of recurrence count. For regions with at least two retained estimates, we compared the highest and lowest values to assess variation among dates. Confidence intervals and resampling procedures are described in Supplementary Section S6.

2.6. Statistical and geometric properties of three key steps

The workflow converts recurrence, spatial grouping and emission-rate estimation into detection frequency, candidate source regions and cross-sectional fluxes, respectively. The following statements define the direct meaning of these quantities. Detection frequency compares repeat detections among usable observing opportunities; fixed-centre grouping defines the spatial extent of a candidate source region; and polygon-CSF geometry reduces pixel-discretization effects without replacing background or wind quality control. Full assumptions, derivations and synthetic tests are provided in Supplementary Section S11.

2.6.1. Detection frequency describes mean detectability under the specified observing conditions

For source region i, let K_i be the number of detections during N_i valid observing opportunities. The detection frequency is defined by Eq. (3):

$$\widehat{r}_i = \frac{K_i}{N_i}. \tag{3}$$

If detection outcomes are conditionally independent after the observing conditions of each overpass are taken into account, and the detection probability p_it can differ among overpasses, then Eq. (4) holds:

$$E(\widehat{r}_i) = \bar{p}_i = \frac{1}{N_i}\sum_{t=1}^{N_i} p_{it}. \tag{4}$$

Thus, K_i/N_i estimates the mean detectability of that location under the data-quality, coverage and detection rules used here. It is not the fraction of time during which the source actually emits. For independent bounded detection outcomes, Hoeffding's inequality further gives Eq. (5) [32].

$$\Pr\left(|\widehat{r}_i - \bar{p}_i| \geq \varepsilon\right) \leq 2\exp\left(-2N_i\varepsilon^2\right). \tag{5}$$

Under the stated independence assumption, random variation caused by finite sampling decreases as the number of valid observing opportunities increases. We use detection frequency to reduce the influence of geographic differences in satellite sampling, not as an estimate of emission activity.

2.6.2. *Fixed-centre grouping bounds the spatial extent of a candidate source region*

Let c be the fixed centre of a candidate source region and r its grouping radius, such that every independent enhancement location x satisfies d(x,c) ≤ r. By the triangle inequality, any two members x and y satisfy

$$d(x, y) \leq d(x, c) + d(y, c) \leq 2r. \tag{6}$$

The maximum within-region distance is therefore no greater than 2r. With r = 25 km, the maximum distance between any two observations assigned to the same candidate source region is 50 km. This bound follows from keeping the centre fixed after it is established; it prevents unbounded chaining through successive local neighbours. It defines the spatial extent of the grouping rule, not an assertion that 25 km is optimal for every physical source or localization error.

2.6.3. *The polygon-CSF integration error can be separated into three components*

Let L denote a complete transect and I its true background-subtracted integral. Let L_obs denote the part covered by valid pixels and G the uncovered remainder. Suppose that the local CO column field satisfies a Lipschitz condition with constant L_Ω, the maximum pixel diameter is h, the background-estimation error is bounded by b, and the background-subtracted enhancement over the uncovered part is bounded by M_G. The integral Î calculated from the actual intersection lengths of the pixel polygons then satisfies Eq. (7):

$$|\widehat{I} - I| \leq L_\Omega h|L_{\mathrm{obs}}| + b|L_{\mathrm{obs}}| + M_G|G|. \tag{7}$$

The three terms correspond to pixel discretization, background estimation and missing transect coverage. Actual pixel–transect intersection lengths primarily reduce the first term; they do not remove background or missing-coverage errors. Because the emission rate is also multiplied by wind speed, wind-speed error enters Q multiplicatively. This decomposition identifies error sources under explicit assumptions; it is not an empirical guarantee of the absolute error for every real estimate.

2.7. *Six industrial case studies*

Six cases were selected from the 180 regions used for industrial-composition and emission-rate analyses, to illustrate different industrial sectors and spatial configurations. For each case, we show the original CO total column, the corrected local enhancement and the delineated footprint. The footprint is also overlaid on high-resolution imagery of the industrial area, together with a closer view centred on the principal facilities. The imagery is used only to examine the spatial relationship between the enhancement and ground facilities; it does not enter the automated search or the emission-rate calculation.

3. Results

3.1. The global catalogue contained 13,363 candidate source regions

The automated workflow processed 20,279 TROPOMI Level-2 CO product files from 2020 to 2023. After overlapping detections from the same satellite overpass were merged, 25,587 independent enhancement observations remained. Grouping these observations by location produced 13,363 candidate source regions. Facility coordinates did not enter this search and were introduced only after the source regions had been identified.

Of the 13,363 regions, 8,377 were observed once, 4,172 were observed 2-4 times, 646 were observed 5-9 times and 168 were observed at least 10 times. The catalogue thus retains single-observation locations for follow-up while separating 4,986 regions observed at least twice, including 814 observed at least five times.

3.2. A small subset of source regions recurred across all four years

The catalogue contained 168 regions detected during at least 10 different satellite overpasses (Fig. 5). They occurred on several continents and were concentrated particularly in East, South and Central Asia. Recurrence count is the number of overpasses during which TROPOMI detected an enhancement, and describes repeated detection rather than the duration of emissions.

Because the number of usable TROPOMI overpasses differs among locations, cumulative counts alone cannot exclude sampling differences. We therefore calculated detection frequency, the proportion of overpasses with basic observing conditions in which a source region was detected. Median detection frequencies for regions observed once, 2-4 times, 5-9 times and at least 10 times were 0.29%, 0.66%, 1.55% and 3.48%, respectively. After valid observing opportunities were included in the denominator, the typical detection frequency of regions observed at least 10 times remained approximately 12 times that of regions observed once. High recurrence was therefore not simply a consequence of more frequent satellite coverage.

The regions observed at least 10 times were also not products of dense sampling in a single year. Of the 168 regions, 134 were detected in all four years from 2020 through 2023, 31 were detected in three years and the remaining three in two years. The high-recurrence tail was therefore dominated by locations that recurred across years and formed the part of the global catalogue most suitable for priority monitoring.

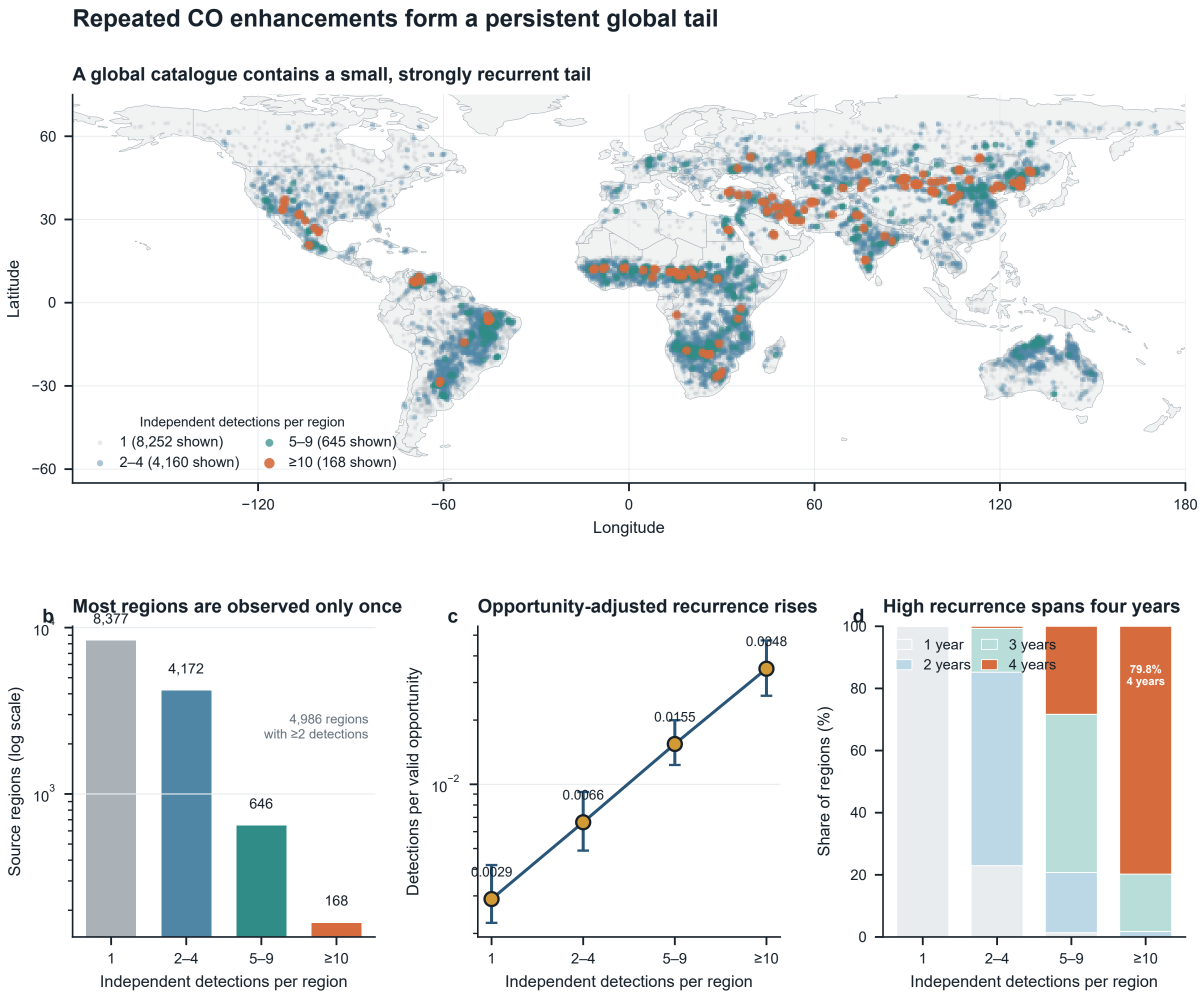

Figure 5: A small number of CO source regions recur across multiple years. The 13,363 candidate source regions identified during 2020–2023 are shown, with regions having more detections plotted above single-detection regions (a). Four mutually exclusive groups contain 8,377, 4,172, 646 and 168 regions detected once, 2–4 times, 5–9 times and at least 10 times, respectively (b). The median proportions of re-detected enhancements during valid satellite overpasses are 0.29%, 0.66%, 1.55% and 3.48% for the four groups, respectively; points and error bars show medians and interquartile ranges (c). Of the 168 regions detected at least 10 times, 134 (79.8%) were detected in every year from 2020 to 2023 (d).

3.3. Stronger recurrence was increasingly associated with industrial environments

The proportion of regions with a nearby industrial-facility record increased with recurrence (Fig. 6). Among all 13,363 source regions, 5,701 had at least one facility record within 25 km of the enhancement footprint. This proportion rose from 38.1% for regions observed once to 47.9% for those observed 2-4 times, 58.8% for those observed 5-9 times and 81.0% for those observed at least 10 times. Because facility coordinates were not used in the automated search, this gradient emerged only when the completed source-region catalogue was compared with external facility records.

More recurrent regions not only occurred near facilities more often, but also contained more facility records at shorter distances. Among the 5,701 facility-associated regions, the median numbers of distinct facility names across the four recurrence groups were 4, 6, 9 and 13.5, respectively. Median distance from the enhancement footprint to the nearest facility declined from 3.99 to 2.40, 1.23 and 0.55 km. Thus, from single-observation regions to regions observed at least 10 times, the typical number of nearby facilities more than tripled while the nearest-facility distance fell to approximately one-seventh.

These relationships were not explained simply by more frequent satellite coverage in some regions or by denser local catalogues. Regression models accounted for valid observing opportunities, latitude, continent, local facility-record density and enhancement quality. Each doubling of recurrence count was associated with 20.2% more nearby facilities (95% confidence interval, 17.0%-23.5%) and a 32.1% shorter nearest-facility distance (30.0%-34.2%). The direction of both relationships was unchanged after facilities with the same name within 5 km were merged and when the analysis was restricted to Global Energy Monitor records. The results consistently support the conclusion that more recurrent CO enhancements are increasingly concentrated in facility-dense industrial environments.

The automated search also rediscovered six industrial CO areas previously reported in satellite studies: Baotou-Jiuyuan, Fushun, the Jindal plant, Duisburg-Schwelgern, Ostrava-Trinec and Dillingen [7, 12, 16]. These locations were not used for model training, candidate generation or threshold selection, yet a corresponding source region was found within 25 km of each and five were observed at least five times. Rediscovery without a location cue provides external location-level support that the global search can recover industrial CO areas identified in previous studies.

3.4. Most regions in the highest industrial-evidence tier were multi-facility industrial areas

Among the 13,363 candidate source regions, 180 met the predefined highest industrial-evidence criteria: at least five enhancements occurred near industrial facilities, while the corresponding dates had complete active-fire coverage and no matched fire. These 180 regions were used for industrial-composition and instantaneous emission-rate analyses. Of these, 127 were in Asia; China contained 63, Iran 18, and Kazakhstan and the United States 13 each.

Facility catalogues showed that most of these 180 regions were located in industrial areas containing several facility types. Combustion or power-generation facilities occurred in 170 regions, cement facilities in 123, oil and gas facilities in 122, iron and steel facilities in 94 and coal mines in 65. These are non-exclusive context labels: one source region can contain several facility types, so the counts are not mutually exclusive sector shares.

The sectoral composition differed among countries. The 63 Chinese regions most commonly contained combustion or power-generation, iron and steel, cement and coal-mining facilities; the 18 Iranian regions mainly involved combustion or power generation, cement, oil and gas, and iron and steel; and the 13 Kazakhstani regions commonly contained combustion or power generation, oil and gas, iron and steel, cement and coal mining. Recurrent CO enhancements were therefore associated with several combinations of heavy-industry activities rather than one sector alone.

Rather than assigning the nearest facility as the unique source, we summarized the sectoral information around each enhancement footprint. Of the 180 regions, 136 (75.6%) contained multiple industrial facility types, 37 had evidence of industrial activity but unresolved sectoral composition and only seven were dominated by one sector. At the TROPOMI observation scale, most of these regions are therefore more appropriately interpreted as industrial areas or facility groups than as isolated individual plants.

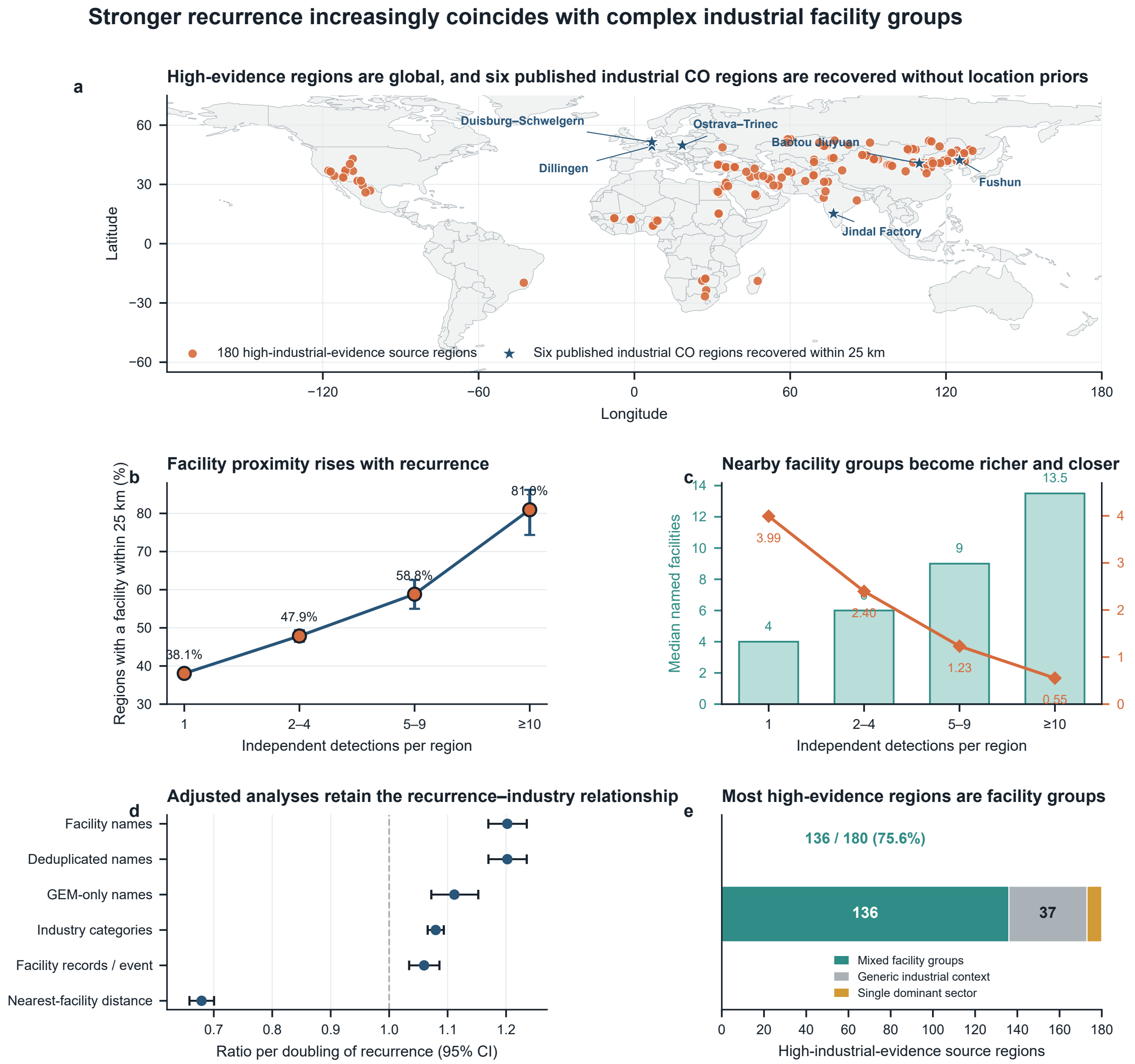

Figure 6: The more frequently an enhancement occurs, the more often it is near an industrial area containing multiple facility types. The 180 source regions retained after facility and same-day active-fire screening for industrial-composition and emission-rate analyses, together with six industrial CO areas reported in previous studies and rediscovered by the present method without location hints (a). The proportion of candidate source regions with a facility record within 25 km increases from 38.1% for single-detection regions to 81.0% for regions detected at least 10 times; error bars show 95% confidence intervals for the binomial proportion using the Wilson method (b). In the same group order, the median number of different facility names nearby increases from 4 to 13.5, while the median distance from the enhancement extent to the nearest facility decreases from 3.99 km to 0.55 km (c). These relationships remain after accounting simultaneously for satellite observing opportunities, geographic location, local facility-record density and enhancement quality; the ratios in the figure show the average change and 95% confidence interval in facility count and nearest-facility distance for each doubling of recurrence count (d). Among the 180 regions, 136 contain multiple industrial facility types, 37 have evidence of industrial facilities but an unknown sectoral composition, and 7 are dominated by a single sector (e).

3.5. Conditional emission rates provide information complementary to recurrence

Of the 180 regions, 177 had at least one overpass that met the image and wind requirements for a conditional instantaneous emission-rate estimate. A total of 512 overpasses were retained (Fig. 7), covering 98.3% of the 180 regions. We first calculated the median of repeated estimates for each region and then compared the 177 region-level values. Their median emission rate was 35.0 Mg h^{-1}, with an interquartile range of 23.6-49.3 Mg h^{-1}. This distribution describes the magnitude during qualifying satellite overpasses.

We next asked whether a more recurrent region also had a higher instantaneous emission rate. It did not. Recurrence count was almost unrelated to the region-level median emission rate (Spearman ρ = -0.0176, n = 177); replacing recurrence count with detection frequency did not change the result (Supplementary Section S6). Recurrence answers how often a location was detected, whereas the conditional emission rate describes how strong the enhancement was during a qualifying overpass; neither quantity replaces the other.

Estimates also varied among dates within the same region. Among the 173 regions with at least two retained estimates, the median ratio of the highest to the lowest estimate was 2.26, and 100 regions had a highest estimate more than twice their lowest. A single-overpass estimate should therefore not be treated as a fixed long-term emission rate; repeated estimates describe variation among qualifying observation dates.

To test whether the estimated magnitudes were consistent with previous TROPOMI CO studies, we compared Lahore and Khartoum, which were analysed both here and in the literature. The median estimate for the Lahore region was 28.3 Mg h^{-1}, compared with a published central estimate of 31.7 Mg h^{-1} and a range of 20.5-43.6 Mg h^{-1}. For Khartoum, the corresponding values were 41.0 Mg h^{-1} here and a published central estimate of 45.2 Mg h^{-1} with a range of 38.4-49.3 Mg h^{-1} [9, 31]. Both estimates fell within the respective published ranges, providing two cross-study supports for the CO emission-rate magnitude obtained here. Because the studies used different overpass dates, this is a range-consistency check rather than same-overpass independent validation.

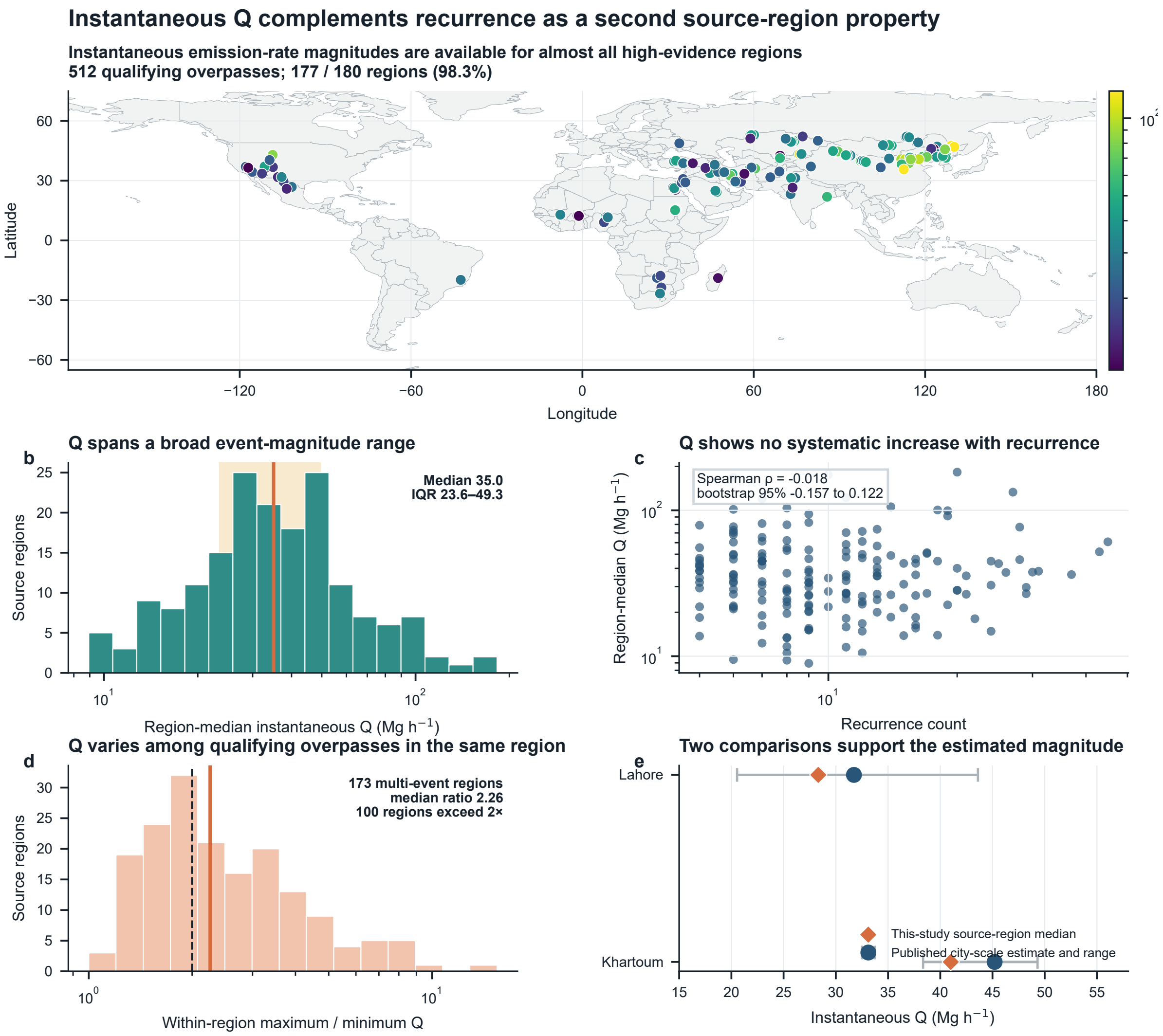

Figure 7: Instantaneous emission rates and their relationship with enhancement recurrence. Of the 180 source regions used for industrial-composition and emission-rate analyses, 177 yielded an instantaneous emission rate during at least one overpass meeting the image and wind requirements, with 512 overpasses retained in total (a). Repeated estimates were first reduced to a median for each source region and then compared across 177 regions; the resulting median was 35.0 Mg h−1, with an interquartile range of 23.6–49.3 Mg h−1 (b). The number of detections in a source region was almost unrelated to its median emission rate (Spearman ρ = −0.018, n = 177) (c). Among the 173 regions with at least two valid emission-rate estimates, the median ratio of the maximum to minimum was 2.26, and the ratio exceeded 2 in 100 regions (d). The estimates for Lahore and Khartoum fall within the city-scale ranges reported by previous TROPOMI cross-sectional-flux studies (e); because the observation dates differ, only the emission-rate ranges are compared here.

3.6. *Six cases place the global result in identifiable industrial areas*

Figures 8 and 9 present six industrial areas in which enhancements were observed repeatedly. For each case, we show the original TROPOMI CO total column, the corrected local enhancement, the delineated enhancement footprint, the footprint overlaid on high-resolution imagery of the industrial area, and a closer facility-centred view. This two-scale presentation places the satellite-observed footprint and its ground industrial context in the same case.

The Jiuquan Iron and Steel complex in China, the Esfahan steel complex in Iran and the Magnitogorsk complex in Russia are large integrated iron and steel sites. Their source regions were observed 20, 25 and 19 times, respectively, and the displayed overpasses had conditional instantaneous emission rates of 28.3, 43.1 and 49.5 Mg h^{-1}. Public sources indicate that all three complexes contain adjacent coking, sintering, ironmaking, steelmaking, rolling and on-site energy-generation stages [22–24, 27, 28]. The enhancement footprints cover several production units rather than one process line, illustrating why the global result is more appropriately interpreted at the industrial-area scale.

Guotai Xinhua in China, Karaganda in Kazakhstan and Mashhad in Iran represent three other industrial systems. Their regions were observed 13, 11 and 12 times, respectively, and the displayed overpasses had conditional instantaneous emission rates of 56.2, 46.6 and 23.6 Mg h^{-1}. Public sources identify Guotai Xinhua as a coal-to-methanol complex with captive coal-fired power generation, Karaganda TPS-3 as a coal-fired combined heat-and-power plant, and Mashhad as a gas-fired power station [25, 26, 29, 30]. Together, the six cases show that the global search identifies different industrial-area configurations: recurrence sets monitoring priority, conditional emission rates describe qualifying overpasses, and the two-scale imagery helps interpret the industrial structure within the observed footprint.

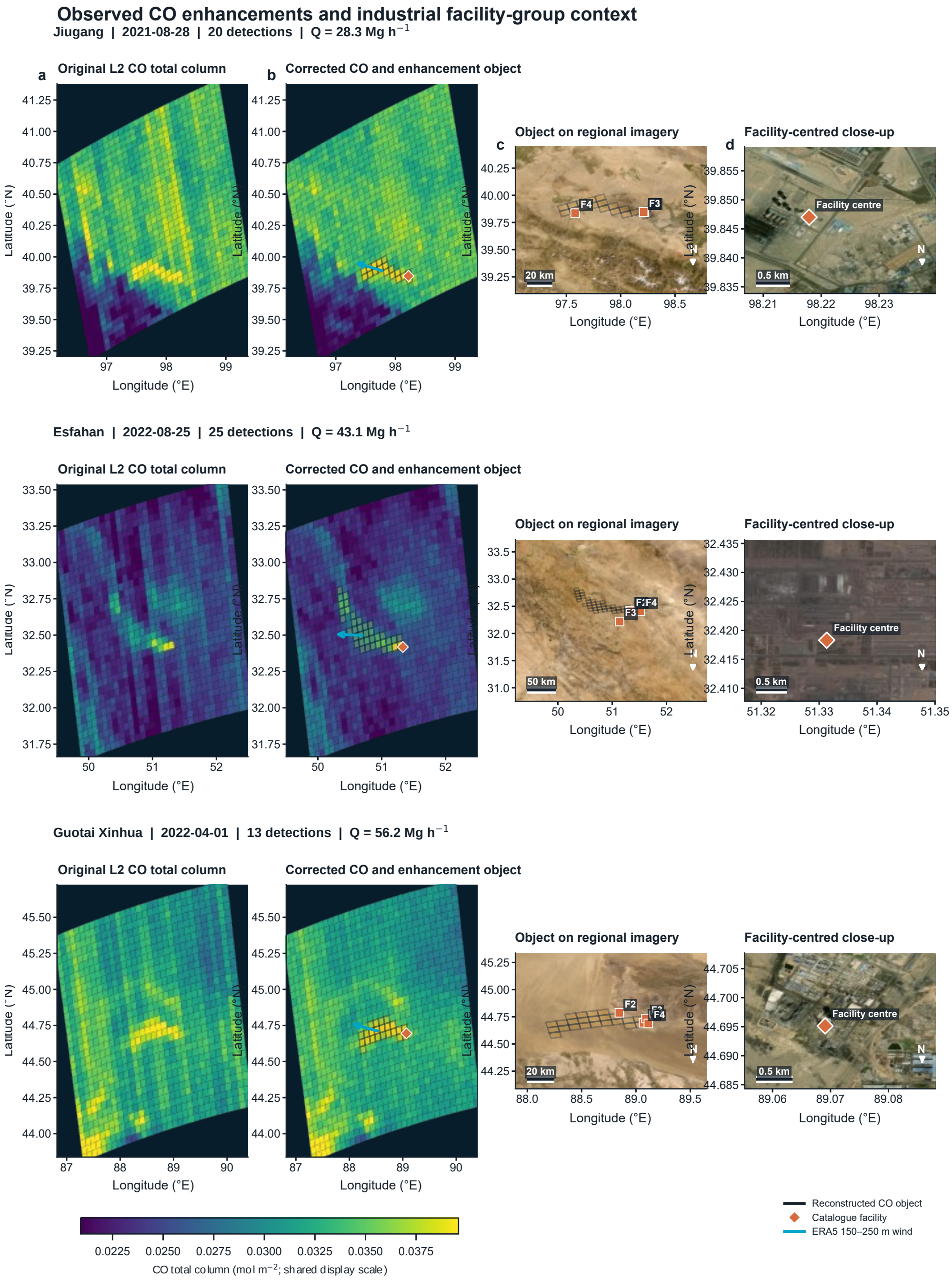

Figure 8: Satellite enhancements and industrial-facility context for Jiugang, Esfahan and Guotai Xinhua. Each case successively shows the original TROPOMI Level-2 CO total column, the corrected CO field and enhancement extent, the complete enhancement extent over high-resolution imagery of the industrial area, and a further enlarged close-up centred on the main facility. Black boundaries and semi-transparent golden fills indicate enhancement extents, orange symbols indicate facility-catalogue locations, and cyan arrows indicate ERA5 wind direction at 150–250 m. Missing pixels in the figure were filled only to improve visual presentation; enhancement delineation, emission-rate calculation and all statistics use the original valid pixels. The high-resolution imagery may have a different date from the TROPOMI overpass and is used to interpret land use and the industrial-facility context. Basemap imagery is from Esri World Imagery; source credits are provided by Esri, Maxar, Earthstar Geographics, and the GIS User Community.

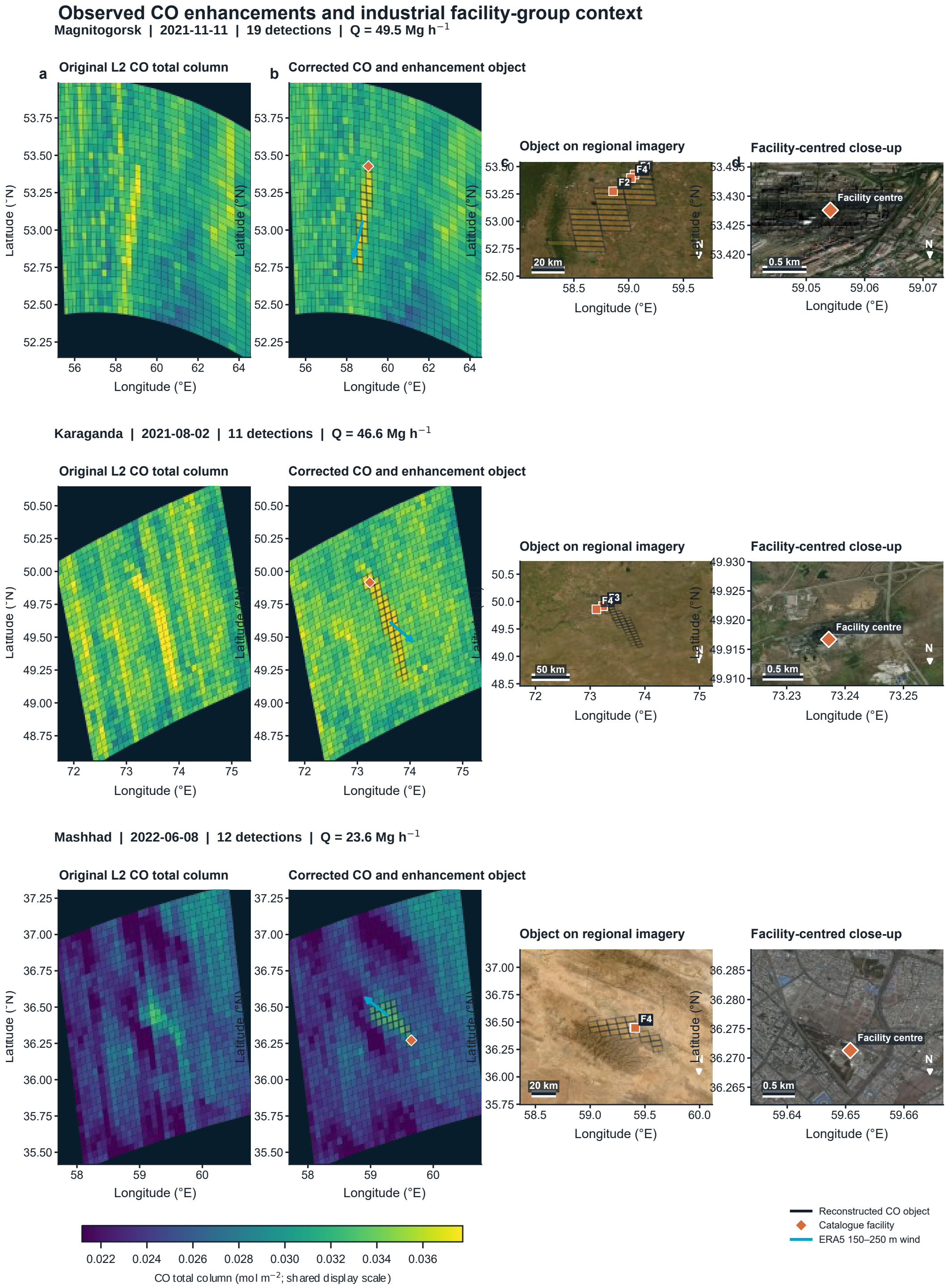

Figure 9: Satellite enhancements and industrial-facility context for Magnitogorsk, Karaganda and Mashhad. The panel arrangement and symbol meanings are the same as in Fig. 8. The three cases show integrated iron and steel, coal-fired combined heat and power, and gas-fired power-generation areas, respectively. The figure retains the CO field actually observed by the satellite, the redefined enhancement extent, the high-resolution background of the entire industrial area and the facility close-up, allowing direct comparison of information at different spatial scales. The six cases illustrate how the global statistical results appear in specific industrial areas. Basemap imagery is from Esri World Imagery; source credits are provided by Esri, Maxar, Earthstar Geographics, and the GIS User Community.

4. Discussion

4.1. Automated global screening extends CO studies that begin from known locations

Previous TROPOMI CO studies generally selected a city or industrial facility first and then defined the background, wind direction and emission rate around that target [7–9, 12, 16]. This strategy is well suited to detailed analysis of known targets. The present workflow moves the search stage earlier: it builds a catalogue of recurrent CO enhancement regions without facility coordinates and introduces facility and active-fire information only after the catalogue has been formed. Facility catalogues are therefore attribution information, not search priors.

The overall strategy was inspired by the global methane study of Schuit et al. [10], which linked automated screening of a large satellite archive with recurrent locations and source analysis. The two studies share the goal of building a reviewable catalogue of recurrent source regions, but they address different observations and localization tasks. Schuit et al. identified methane signals with distinct plume forms and used high-resolution methane satellites for facility localization. Here, the available CO labels are scene-level, so scenes are screened first, enhancement footprints are delineated from observed CO pixels, and observations on different dates are then grouped into source regions. Each task is therefore assigned to the evidence that can support it.

4.2. Recurrence across years identifies source regions that merit further investigation

The value of repeated observations is not simply that the same location is counted several times. After valid observing opportunities were included in the denominator, the typical detection frequency of regions observed at least 10 times remained approximately 12 times that of regions observed once, and 134 of the 168 high-recurrence regions were detected in all four years. High recurrence therefore generally indicates repeated formation of an identifiable CO enhancement at the same location across years, rather than only more frequent satellite coverage. Detection frequency adjusts for observing opportunity and represents mean detectability under the data and detection rules used here; it is not the fraction of time during which the source emits.

Fixed-centre grouping also gives the recurrence statistic a defined spatial scale. A 25-km grouping radius keeps any two observations assigned to one region within 50 km and prevents a chain of local neighbours from extending the region indefinitely. Facility associations strengthened with recurrence, and six industrial CO areas reported in previous studies were rediscovered without location cues. The recurrent-source catalogue therefore provides more than a count: it identifies locations that can be prioritized for industrial follow-up.

4.3. Recurrent facility-associated enhancements generally represent industrial areas rather than single plants

A principal finding is that recurrent enhancements become increasingly concentrated in facility-dense industrial environments. The proportion with a nearby facility record increased from 38.1% to 81.0%, while facility counts increased and nearest-facility distances decreased. Among the 180 regions in the highest industrial-evidence tier, 136 contained multiple industrial facility types. At the spatial scale of TROPOMI, an industrial area or facility group is therefore a more appropriate attribution unit than the nearest individual plant.

This interpretation is consistent with the physical organization of large industrial complexes. Integrated steelworks commonly place coking, sintering, ironmaking, steelmaking, rolling and captive power generation in adjacent areas, while coal-conversion and thermal-power facilities may also be co-located. A single TROPOMI enhancement can cover several such units, so retaining the sectoral combination within the footprint gives a more complete description than assigning the signal to one facility.

The six cases connect this global statistical result to identifiable locations. High-resolution imagery shows several neighbouring facilities within the footprints at Jiuquan, Esfahan and Magnitogorsk, among other examples. The imagery provides land-use and facility context but does not measure CO; together with the global facility statistics and TROPOMI enhancements, it supports industrial-area attribution rather than facility-level truth.

4.4. Recurrence and instantaneous emission rate provide complementary information

Recurrence and conditional instantaneous emission rate describe different aspects of a source region. Among the 177 regions with estimates, recurrence count was nearly unrelated to the region-level median emission rate (ρ = -0.0176), and the result remained unchanged when detection frequency was used. One region may produce moderate detectable enhancements repeatedly, whereas another may show a high estimated rate during only a few qualifying overpasses. Recurrence is therefore suited to selecting locations for continued monitoring, while conditional emission rates describe magnitude during particular overpasses.

Emission estimates within a region also varied markedly among dates: in 100 of the 173 regions with repeated estimates, the highest value exceeded the lowest by more than a factor of two. The Lahore and Khartoum medians fell within ranges reported by previous TROPOMI studies and provide two cross-study supports for the magnitude. The estimates should consequently be interpreted as conditional overpass-scale quantities rather than fixed source strengths.

The polygon-CSF geometry uses actual intersections between pixel polygons and transects, reducing discretization caused by treating irregular pixels as points or regular cells. Background estimation, missing transect coverage and wind speed still affect the result, so the estimates describe instantaneous magnitude for observations meeting the image and wind requirements. They are not converted into annual emissions or treated as a time-invariant source strength.

For practical monitoring, recurrence and conditional emission rate should be used together. Highly recurrent regions are suitable for continued monitoring, high-rate overpasses merit priority review, and regions combining high recurrence with high rates can be placed at the top of a verification list. The surrounding sectoral composition can then guide which industrial activities should be examined.

5. Conclusions

We developed a global workflow for automated identification, industrial attribution and conditional emission-rate quantification of recurrent CO enhancement source regions from TROPOMI observations. Facility coordinates were not used during the search. Processing 20,279 Level-2 product files from 2020 to 2023 yielded 25,587 independent enhancement observations, which were grouped into 13,363 candidate source regions. Of these, 4,986 were observed at least twice and 168 at least 10 times; 134 of the high-recurrence regions were detected in all four years.

Recurrent enhancements were increasingly concentrated in facility-dense industrial environments. The proportion with a nearby facility record rose from 38.1% for single-observation regions to 81.0% for regions observed at least 10 times, while nearby facility counts increased and nearest-facility distances decreased. Among the 180 regions in the highest industrial-evidence tier, 136 contained multiple industrial facility types. Most recurrent enhancements are therefore more appropriately interpreted as industrial-area or facility-group signals than assigned directly to individual plants.

For overpasses meeting the image and wind requirements, polygon-CSF produced 512 conditional instantaneous emission-rate estimates across 177 regions, with a region-level median of 35.0 Mg h^{-1}. Recurrence was not equivalent to emission rate, so persistent locations and high-rate overpasses must be identified separately. The Lahore and Khartoum comparisons provide two cross-study magnitude supports. By searching globally before introducing facility locations, the workflow links CO-enhancement discovery, industrial attribution and conditional emission-rate quantification, providing a practical way to prioritize industrial areas for verification and continued monitoring.

CRediT authorship contribution statement

Haoyi Wu: Conceptualization, Methodology, Software, Data curation, Formal analysis, Investigation, Visualization, Writing – original draft, Writing – review and editing, Project administration. Renwei Meng: Conceptualization, Validation, Writing – review and editing.

Funding

This research did not receive any specific grant from funding agencies in the public, commercial, or not-for-profit sectors.

Declaration of competing interest

The authors declare no known competing financial interests or personal relationships that could have appeared to influence the work.

Data availability

TROPOMI Level-2 CO, ERA5, NASA FIRMS and cited public facility catalogues are obtained from their respective providers. The AutoMerge CO weak-label dataset is archived at Zenodo, DOI 10.5281/zenodo.17226619. Derived tables and provenance records are available from the corresponding author upon reasonable request.

Code availability

The analysis scripts and frozen configuration are maintained in a private repository. Confidential access can be provided to the editor and reviewers upon reasonable request, and the repository is planned for public release following publication.

Declaration of generative AI and AI-assisted technologies in the writing process

During the preparation of this work, the authors used OpenAI ChatGPT and Codex for English translation, language editing, document formatting, and layout assistance for explanatory workflow diagrams. The authors reviewed and edited all outputs and take full responsibility for the content of the article. These tools were not used to generate or alter primary satellite observations, derived numerical results, or statistical analyses.

References

[1] Veefkind, J. P. et al. TROPOMI on the ESA Sentinel-5 Precursor: A GMES mission for global observations of the atmospheric composition for climate, air quality and ozone layer applications. Remote Sensing of Environment 120, 70-83 (2012). https://doi.org/10.1016/j.rse.2011.09.027

[2] Landgraf, J. et al. Carbon monoxide total column retrievals from TROPOMI shortwave infrared measurements. Atmospheric Measurement Techniques 9, 4955-4975 (2016). https://doi.org/10.5194/amt-9-4955-2016

[3] Borsdorff, T. et al. Measuring carbon monoxide with TROPOMI: First results and a comparison with ECMWF-IFS analysis data. Geophysical Research Letters 45, 2826-2832 (2018). https://doi.org/10.1002/2018GL077045

[4] Sha, M. K. et al. Validation of methane and carbon monoxide from Sentinel-5 Precursor using TCCON and NDACC-IRWG stations. Atmospheric Measurement Techniques 14, 6249-6304 (2021). https://doi.org/10.5194/amt-14-6249-2021

[5] Borsdorff, T. et al. Improving the TROPOMI CO data product: update of the spectroscopic database and destriping of single orbits. Atmospheric Measurement Techniques 12, 5443-5455 (2019). https://doi.org/10.5194/amt-12-5443-2019

[6] Lin, P. et al. TROPOMI unravels transboundary transport pathways of atmospheric carbon monoxide in Tibetan Plateau. Science of the Total Environment 952, 175942 (2024). https://doi.org/10.1016/j.scitotenv.2024.175942

[7] Tian, Y. et al. Satellite observations reveal a large CO emission discrepancy from industrial point sources over China. Geophysical Research Letters 49, e2021GL097312 (2022). https://doi.org/10.1029/2021GL097312

[8] Goudar, M., Anema, J. C. S., Kumar, R., Borsdorff, T. & Landgraf, J. Plume detection and emission estimate for biomass burning plumes from TROPOMI carbon monoxide observations using APE v1.1. Geoscientific Model Development 16, 4835-4852 (2023). https://doi.org/10.5194/gmd-16-4835-2023

[9] Leguijt, G. et al. Quantification of carbon monoxide emissions from African cities using TROPOMI. Atmospheric Chemistry and Physics 23, 8899-8919 (2023). https://doi.org/10.5194/acp-23-8899-2023

[10] Schuit, B. J. et al. Automated detection and monitoring of methane super-emitters using satellite data. Atmospheric Chemistry and Physics 23, 9071-9098 (2023). https://doi.org/10.5194/acp-23-9071-2023

[11] Wąsala, J. et al. AutoMergeNet: AutoML-based M-source satellite data fusion evaluated with atmospheric case studies. IEEE Journal of Selected Topics in Applied Earth Observations and Remote Sensing 18, 26613-26625 (2025). https://doi.org/10.1109/JSTARS.2025.3621068

[12] Leguijt, G. et al. Comparing space-based to reported carbon monoxide emission estimates for Europe's iron and steel plants. Atmospheric Chemistry and Physics 25, 555-574 (2025). https://doi.org/10.5194/acp-25-555-2025

[13] Schroeder, W., Oliva, P., Giglio, L. & Csiszar, I. A. The new VIIRS 375 m active fire detection data product: Algorithm description and initial assessment. Remote Sensing of Environment 143, 85-96 (2014). https://doi.org/10.1016/j.rse.2013.12.008

[14] Hersbach, H. et al. The ERA5 global reanalysis. Quarterly Journal of the Royal Meteorological Society 146, 1999-2049 (2020). https://doi.org/10.1002/qj.3803

[15] Sentinel-5P Mission Performance Centre. Carbon Monoxide [L2_CO___] Readme, document S5P-MPC-SRON-PRF-CO, issue 2.5, product version V02.05.00 (2023). https://sentinels.copernicus.eu/documents/247904/3541451/Sentinel-5P-Carbon-Monoxide-Level-2-Product-Readme-File

[16] Tian, Y. et al. Quantifying CO emission rates of industrial point sources from Tropospheric Monitoring Instrument observations. Environmental Research Letters 17, 014057 (2022). https://doi.org/10.1088/1748-9326/ac3b1a

[17] Pinheiro, P. O. & Collobert, R. From image-level to pixel-level labeling with convolutional networks. In Proceedings of the IEEE Conference on Computer Vision and Pattern Recognition, 1713-1721 (2015). https://doi.org/10.1109/CVPR.2015.7298780

[18] Choe, J. et al. Evaluating weakly supervised object localization methods right. In Proceedings of the IEEE/CVF Conference on Computer Vision and Pattern Recognition, 3133-3142 (2020). https://doi.org/10.1109/CVPR42600.2020.00320

[19] Wang, H. et al. MOL: Towards accurate weakly supervised remote sensing object detection via multi-view noisy learning. ISPRS Journal of Photogrammetry and Remote Sensing 196, 457-470 (2023). https://doi.org/10.1016/j.isprsjprs.2023.01.011

[20] Ilse, M., Tomczak, J. & Welling, M. Attention-based deep multiple instance learning. In Proceedings of the 35th International Conference on Machine Learning, PMLR 80, 2127-2136 (2018). https://proceedings.mlr.press/v80/ilse18a.html

[21] Wąsala, J. et al. Carbon monoxide plume detection dataset for machine learning, version 1.0.0. Zenodo (2025). https://doi.org/10.5281/zenodo.17226619

[22] Jiuquan Iron and Steel (Group) Co., Ltd. Industrial sectors: iron and steel. https://www.jiugang.com/industry/content/1 (accessed 21 July 2026).

[23] Global Energy Monitor. Jiugang Group Captive Gas power station. https://www.gem.wiki/Jiugang_Group_Captive_Gas_power_station (accessed 21 July 2026).

[24] Global Energy Monitor. Esfahan Steel Isfahan plant. https://www.gem.wiki/Esfahan_Steel_Isfahan_plant (accessed 28 July 2026).

[25] Global Energy Monitor. Xinjiang Guotai Xinhua Coal-to-Methanol Plant. https://www.gem.wiki/Xinjiang_Guotai_Xinhua_Coal-to-Methanol_Plant (accessed 21 July 2026).

[26] Global Energy Monitor. Guotai Xinhua Coal Chemical power station. https://www.gem.wiki/Guotai_Xinhua_Coal_Chemical_power_station (accessed 21 July 2026).

[27] Global Energy Monitor. Magnitogorsk Iron and Steel Works. https://www.gem.wiki/Magnitogorsk_Iron_and_Steel_Works (accessed 21 July 2026).

[28] Global Energy Monitor. Magnitogorskaya CHP power station. https://www.gem.wiki/Magnitogorsk_PVS-2_MMK_power_station (accessed 21 July 2026).

[29] Global Energy Monitor. Karaganda-3 power station. https://www.gem.wiki/Karaganda_TPS-3_power_station (accessed 21 July 2026).

[30] Global Energy Monitor. Mashhad power station. https://www.gem.wiki/Mashhad_power_station (accessed 21 July 2026).

[31] Leguijt, G. et al. Characterizing point-source carbon emissions by combining TROPOMI CO and OCO CO2 data. Journal of Geophysical Research: Atmospheres 131, e2025JD044636 (2026). https://doi.org/10.1029/2025JD044636

[32] Hoeffding, W. Probability inequalities for sums of bounded random variables. Journal of the American Statistical Association 58, 13-30 (1963). https://doi.org/10.1080/01621459.1963.10500830

Supplementary Information

Automated identification, industrial attribution and conditional emission-rate quantification of recurrent CO enhancement source regions

Haoyi Wu[a,1,*], Renwei Meng[a,2]

[a]Stony Brook Institute at Anhui University, No. 3 Feixi Road, Shushan District, Hefei, Anhui 230039, China

---

This supplement expands only the single processing chain used in the manuscript. All counts refer to the same four-year product: 20,279 TROPOMI Level-2 file records, 25,587 independent overpass events, and 13,363 candidate source regions. Models not used in the reported workflow, earlier sample counts, and alternative Q calculations are not merged with these results. Product-quality conditions, validation-selected operating points, and operational definitions are distinguished explicitly.

S1. Study Design, Observations, and Statistical Units

The analysis used TROPOMI CO observations from 2020-2023. The annual lists contained 5,186, 5,014, 4,913, and 5,166 Level-2 file records, respectively, for a total of 20,279 records. Paths were unique within and across years and were checked for readability before processing. The principal variables were the CO total column, `qa_value`, pixel centre and corner coordinates, and the product-provided corrected CO field. Local enhancement analysis used `carbonmonoxide_total_column_corrected`, which applies the product-level correction for single-orbit striping [5]. All files entering the four-year result contained this field, so the product did not mix corrected CO with a custom destriping estimate.

The discovery stage used finite CO pixels with `qa_value` >= 0.5 to estimate local backgrounds and reconstruct objects. `qa_value` is a retrieval-quality indicator affected by cloud, albedo, aerosols, and convergence; it is not a plume probability. The broad discovery condition preserves local structure for an unknown-location search. External data entered only after their relevant statistical unit had been formed. ERA5 supplied event-time winds for conditional flux calculations [14]. Global and national facility catalogues supplied industrial context. VIIRS FIRMS supplied same-day active-fire context [13]. None of these data were inputs to candidate generation, PG37-MIL, object reconstruction, CEQ-36, or recurrence grouping.

The search domain was restricted to land and near-coastal locations within 65 degrees latitude. A candidate centre was retained when at least one of nine samples, consisting of the centre and eight samples offset by plus or minus 0.15 degrees in latitude and longitude, intersected the land mask. This is a reproducible angular domain definition rather than a physical plume threshold or a constant-distance coastline buffer.

*Corresponding author

Email addresses: r32314010@stu.ahu.edu.cn (Haoyi Wu), r32314095@stu.ahu.edu.cn (Renwei Meng)

[1]ORCID: 0009-0007-5022-4925

[2]ORCID: 0009-0001-6879-6629

Four statistical units were kept distinct. A scene is a 32 x 32 local window evaluated by the weakly supervised model. A proposal is a local connected enhancement candidate used as a model instance. A reconstructed enhancement object is the deterministic set of corrected-CO pixels used downstream. An independent overpass event is the highest-ranked object for a unique source-region, observation-start-time, and orbit combination. A candidate source region is a fixed-centre spatial group containing one or more independent events. Because one orbital file can produce multiple scenes and one scene can produce multiple proposals, intermediate counts are not expected to form a monotonically decreasing funnel.

S2. Local Candidate Generation and PG37-MIL Screening

Orbital pre-screening was deliberately permissive. On finite positive-CO pixels with finite `qa_value` >= 0.5, missing values were temporarily replaced by the orbit-wide valid-CO median to calculate a 15 x 15 local median. The original missing mask was restored immediately after background estimation. Positive background-subtracted enhancements were smoothed with a Gaussian sigma of 0.5 pixel and transformed to a robust standardized anomaly using the median and median absolute deviation. Pixels with orbit-scale z >= 2.0 formed seeds, and eight-neighbour pixels with z >= 1.0 formed connected extensions. A 3 x 3 closing followed by an opening connected one-pixel gaps and removed isolated noise. Only obviously degenerate structures, such as extremely small, line-like, nearly full-window, strongly fragmented, or non-contrasting components, were rejected at this stage. These rules propose computation windows; they do not constitute final artefact rejection or universal plume morphology.

Missingness was evaluated over three nested domains. The valid-pixel fractions in the 64 x 64 background context, the 32 x 32 model scene, and a proposal-neighbourhood box expanded by six pixels were required to be at least 0.80, 0.80, and 0.85, respectively. The three fractions test broad background support, actual model input support, and truncation around the candidate object. They were evaluated individually and jointly in the sensitivity analysis.

Within each 32 x 32 scene, a new local median and robust scale were calculated. A median absolute deviation of zero triggered a standard-deviation fallback, and the scale was bounded below by 1e-9. Scene-level z >= 2.0 pixels formed proposal cores and connected z >= 1.0 pixels formed their extensions. Each proposal contained at least three pixels and one core pixel. Missing CO pixels could not connect components. QA and retrieval conditions were retained as features rather than used to create hidden connectivity.

The training set contains image-level plume-like/no-plume labels but no instance or pixel labels. Each scene was therefore treated as a labelled bag and its proposals as unlabelled instances. A shared 37-32-16-1 network produced proposal logits. Two hidden layers with 32 and 16 units used ReLU activations and 0.2 dropout. A bag-size-corrected log-sum-exp pooling operation with temperature one produced the scene logit. This aggregation emphasizes the strongest supporting instances without allowing the number of proposals alone to increase a scene score.

Each proposal was represented by 37 reproducible features. Seventeen CO and morphology features described area, core fraction, compactness, elongation, standardized anomaly, and background-subtracted CO. Thirteen quality and retrieval features described QA, missingness, precision, albedo, and scattering conditions. Seven location and swath features described within-scene position, cross-track position, and broad background structure. Wind, facility records, fire detections, year, recurrence, and Q were excluded. Training used 3,319 scenes, validation used 830, and the one-time test set contained 1,058 scenes. BCEWithLogitsLoss and AdamW were used with a learning rate of 0.001, weight decay of 0.0001, batch size 128, and 60 epochs. Seeds 21-25 were compared using validation data only.

Two operating points were fixed on the validation set. The discovery threshold, 0.283247, maximized F1 among thresholds with recall at least 0.80. The high-support threshold, 0.772097, maximized recall among thresholds with precision at least 0.90. The first is the product entry point; the second is a nested conservative indicator. Test predictions were not used to tune either threshold. After a scene passed, all quality-eligible proposals were scored, and the highest-scoring object was propagated in the main product. A Top-3 path was run only as a multi-object sensitivity analysis.

S3. Deterministic CO Object Reconstruction and CEQ-36 Ranking

PG37-MIL decides which proposal deserves priority, not which pixels are used downstream. Pixel membership was reconstructed from corrected CO. The highest finite z pixel with `qa_value` >= 0.5 inside the proposal bounding box was used as a seed. Eight-neighbour growth then included all connected valid pixels with scene-level z >= 1.7 over the full 32 x 32 scene. The resulting component also had to contain at least one z >= 2.4 core pixel inside the original proposal box. The box determines the core location but does not truncate a connected extension or merge a disconnected enhancement elsewhere in the scene.

Missing pixels were neither interpolated nor bridged. If no valid seed existed, the seed was below the extension threshold, the component was empty, or no high core was present, the record retained an explicit reconstruction-failure status. Successful objects retained pixel indices, corners, centroid, area, and CO statistics. The same pixels were used for facility distance and polygon-CSF. Because no pixel-level truth exists, this reproducible boundary is described as an operational object rather than semantic segmentation.

The extension and core thresholds have different roles. One-factor variants used low = 1.5 or 1.9 with high = 2.4, and high = 2.2 or 2.6 with low = 1.7. All variants were compared on reconstruction success, area, Jaccard overlap, centroid displacement, and downstream source-region counts. The 1.7/2.4 pair was retained as a compromise between a clear high-valued origin and connected weaker margins, not as a universal physical threshold.

CEQ-36 ranks whether a reconstructed object has a clear body and a sufficiently clean background for recurrence and conditional quantification. Expert labels used four ordered levels: T1, clear object and clean background; T2, minor missingness or background disturbance but a recognizable enhancement; T3, substantial degradation of either the object or background; and T4, both poor or reject. Uncertain cases were excluded from training. The labels do not encode industry, fire, or Q.

Of 669 labelled objects, 593 were reconstructable under the common rule. Six duplicate groups were consolidated, leaving 587 unique training objects: 78 T1, 96 T2, 215 T3, and 198 T4. Thirty-six features described core concentration, connectivity, fragmentation, compactness, object-to-background contrast, broad background gradient, missingness, QA, albedo, scattering, and retrieval precision. PG scores, coordinates, year, wind, fire, facilities, recurrence, and Q were excluded. An ExtraTrees regressor with 700 trees and a minimum leaf size of three mapped T4/T3/T2/T1 to 0/1/2/3 and produced the continuous CEQ-36 score S_{CEQ}. Missing values were imputed with training-fold medians.

Internal validation used five repeats of five-fold grouped cross-validation, separately grouping by scene, Level-2 product, observation date, and 10-degree spatial block. A temporally blind set contained 30 randomly selected objects from each of 2020, 2021, and 2022; labels were assigned before model scores were revealed. The principal threshold S_{CEQ} >= 1.50 is the midpoint between T2 and T3 on the encoded scale. Thresholds of 1.25 and 1.75 form relaxed and strict sensitivity layers. The score is an expert-usability ranking, not a plume probability.

S4. Independent Events and Fixed-Centre Recurrent Regions

Objects passing the principal usability point were sorted by S_{CEQ}, PG scene score, PG proposal score, and summed standardized anomaly, with an object identifier resolving exact ties. The first unassigned object created a fixed centre. Subsequent objects joined that group only when they were within 25 km of the centre; the centre never moved and every member was directly within the radius. This avoids transitive single-linkage chains that can connect remote endpoints.

Within each preliminary group, only the highest-ranked object for each observation-start-time and orbit combination was retained as an independent overpass event. The resulting groups are candidate source regions. All regions containing at least one event are kept, while ge2, ge5, and ge10 identify nested recurrence levels with at least 2, 5, and 10 independent events. The main radius is an operational TROPOMI-scale definition. Fifteen- and 35-km variants quantify splitting and merging, and reverse and five fixed-random input orders quantify order dependence. Recurrence indicates repeated enhancement observations near a location; it does not measure continuous emission time.

S5. Facility Proximity and Same-Day Active-Fire Evidence

Source context was attached only after source regions had been formed. The facility search database contained 103,608 traceable catalogue records: 46,255 records from GEM and WRI global energy, power, and heavy-industry catalogues and 57,353 public facility-level CO records from the US EPA 2020 NEI, Australian NPI, and Canadian NPRI. Records were deduplicated within each source using stable identifiers, but cross-catalogue records were preserved to retain provenance and co-located entries. The total is therefore a record count rather than the number of unique facilities worldwide.

For each independent event, an initial spherical query found candidate facilities within 50 km plus the object radius. The exact great-circle distance from each candidate facility to every reconstructed-object pixel centre was then calculated. An event received Facility25 context when the minimum distance was at most 25 km, and all records in range were preserved. The 50-km pre-query only reduces computation. The principal 25-km radius and 10/50-km comparisons describe proximity, not causal attribution or a unique emitting facility.

Same-day fire screening was performed for Facility25 events using the VIIRS S-NPP and NOAA-20 FIRMS 375-m products. A zero-hit event was called same-day fire unmatched only when both sensor requests succeeded and the returned geometry fully covered the 25-km search circle. Any active-fire record inside the circle produced a hit. A failed request or incomplete search circle produced an incomplete status, because a zero result under incomplete coverage cannot be interpreted as no fire. A 50-km layer provides broader context but does not replace the main 25-km state.

At source-region level, A, B, and C identify at least 5, 2-4, and 1 independent Facility25 events with complete search circles and no same-day fire match. D indicates facility context without such complete unmatched evidence, and U indicates no facility record within 25 km of any member object. These five classes are mutually exclusive and exhaustive. They are evidence-priority tiers, not source probabilities: D can contain fire-hit or incompletely screened events, and U can reflect catalogue omissions.

S6. Conditional Polygon-Based Cross-Sectional Flux

Polygon-CSF is a separate quantitative layer applied after discovery and evidence stratification. Eligible records are events in strict A-tier regions that individually have Facility25 context, a complete FIRMS 25-km search circle, and no same-day fire match. The algorithm additionally requires a reconstructed object, an upwind background, a 150-250 m wind, and usable cross-sections. Failure produces an explicit status and does not remove the source region or trigger a 10-m wind or arbitrary-background fallback.

Each TROPOMI pixel was represented by its product-provided corner coordinates and projected to a local equidistant system centred on the object. The most upwind boundary point of the object polygon was found by projection onto the wind vector. Transects perpendicular to the wind were placed downstream from this point. This geometric anchor is not interpreted as a stack or a retrieved source coordinate. The mismatch angle is the smallest angle between the direction from the upwind boundary point to the object centroid and the ERA5 downwind direction.

The background was the median CO in a $0.30° \times 0.30°$ upwind region using at least five finite pixels with `qa_value` ≥ 0.5. If the initial background was insufficient, paired regions rotated by $\pm 10°$, $\pm 20°$, $\pm 45°$ and $\pm 60°$ were accumulated in a fixed order. Remaining failure was recorded as insufficient background. For transect j, the flux is calculated as

$$Q_j = U M_{\mathrm{CO}} \int_{L_j} (\Omega_{\mathrm{CO}} - \Omega_{\mathrm{bg}})\, \mathrm{d}l. \tag{S1}$$

Here, U is the mean 150–250 m wind speed, M_{CO} is the CO molar mass, and $\mathrm{d}l$ is the actual intersection length between the transect and an observed pixel polygon. The event estimate is the median of all valid transects and is converted to kg h^{-1}.

The reported calculation required a wind speed of at least 1.5 m s-1, mismatch no greater than 60 degrees, transect valid coverage of at least 0.70, and at least three valid transects. At most 20 transects were placed. The first transect was at least the distance corresponding to 0.1 degree or one typical along-wind pixel thickness downstream from the anchor; the terminal position did not exceed the 95th percentile of along-wind object coordinates. Total cross-wind length was the larger of the 0.4-degree equivalent and twice the 90th percentile of absolute cross-wind coordinates. Seventeen scenarios varied wind layer, minimum wind, background extent, transect count, coverage, first-transect position, maximum mismatch, and object boundary. A 1,000-draw propagation separately quantified retrieval precision. These analyses evaluate internal method dependence and do not constitute validation against independent emission truth.

The quantitative table used the ERA5 hour nearest to each recorded event time. We report these values as conditional instantaneous fluxes under this declared time-matching convention; they are not annualized emissions or externally validated absolute rates.

S7. Complete Model-Training and Evaluation Record

S7.1. PG37-MIL

The fixed split contained 3,319 training, 830 validation, and 1,058 test scenes. The instance network was 37-32-16-1 with ReLU, 0.2 dropout, and bag-size-corrected log-sum-exp pooling at temperature one. Training used BCEWithLogitsLoss, AdamW, learning rate 0.001, weight decay 0.0001, batch size 128, and 60 epochs. Model and operating-point selection used validation data only.

- Discovery threshold 0.283247: precision 0.8377, recall 0.8253, F1 0.8315, TP/FP/FN/TN 222/43/47/746.
- High-support threshold 0.772097: precision 0.9318, recall 0.4572, F1 0.6135, TP/FP/FN/TN 123/9/146/780.

The test values evaluate the AutoMerge weak-label domain and are not global plume-detection metrics.

S7.2. CEQ-36

The training table contained 587 unique reconstructable objects after excluding 76 empty/invalid masks and consolidating six duplicate groups. T1/T2/T3/T4 counts were 78/96/215/198. The final ExtraTreesRegressor used 700 trees and a minimum leaf size of three. Grouped repeated cross-validation gave:

- date_group: Spearman 0.745; top-50 T1/T2 fraction 0.972; bottom-50 T3/T4 fraction 1.000.
- orbit_group: Spearman 0.742; top-50 T1/T2 fraction 0.968; bottom-50 T3/T4 fraction 1.000.
- scene_label_id: Spearman 0.750; top-50 T1/T2 fraction 0.960; bottom-50 T3/T4 fraction 1.000.
- spatial_group_10deg: Spearman 0.748; top-50 T1/T2 fraction 0.964; bottom-50 T3/T4 fraction 1.000.

The score-hidden temporal evaluation used 30 random objects from each of 2020-2022. Spearman correlation was 0.814 with a year-stratified 95% bootstrap interval of 0.733-0.868; T1/T2 versus T3/T4 ranking AUC was 0.955. These values support one-expert usability ranking across years and do not provide pixel truth or inter-expert agreement.

S8. One-Factor Comparisons of Operational Definitions

S8.1. Object-boundary variants

Table S1: Object-boundary sensitivity results.

Variant	Low z	High z	Median area (px)	Jaccard	Centroid shift (px)	Score rho	ge5	ge10
low15_ high24	1.5	2.4	22.0	0.857	0.256	0.973	803	165
low17_ high24	1.7	2.4	17.0	1.0	0.0	1.0	814	168
low19_ high24	1.9	2.4	13.0	0.857	0.249	0.957	690	146
low17_ high22	1.7	2.2	17.0	1.0	0.0	1.0	814	168
low17_ high26	1.7	2.6	17.0	1.0	0.0	1.0	797	164

S8.2. Valid-pixel coverage variants

Table S2: Valid-pixel coverage sensitivity results.

Setting	Context	Core	Screen	Top-1 scenes	Event retention	ge5	ge10
all_loose	0.7	0.8	0.7	200519	1.0	814	168
context_loose	0.7	0.85	0.8	160972	1.0	814	168
core_loose	0.8	0.8	0.8	139293	1.0	814	168
screen_loose	0.8	0.85	0.7	126108	1.0	814	168
main	0.8	0.85	0.8	125126	1.0	814	168
context_strict	0.85	0.85	0.8	92134	0.771	568	99
core_strict	0.8	0.9	0.8	98100	0.812	594	111
screen_strict	0.8	0.85	0.85	118048	0.957	763	153
all_strict	0.85	0.9	0.85	76637	0.661	441	79

S8.3. CEQ-36 working-point variants

Table S3: CEQ-36 working-point sensitivity results.

precsf_threshold	ge5	ge10
1.25	1161	253
1.5	814	168
1.75	570	120

S8.4. Fixed-centre radius variants

Table S4: Fixed-centre grouping-radius sensitivity results.

radius_km	ge5	ge10
15	406	60
25	814	168
35	1158	289

The four comparisons isolate object extent, observation support, usability-score truncation, and spatial grouping scale. They quantify behavior around the principal setting and do not select an optimum against unknown truth.

S9. Seventeen One-Factor polygon-CSF Settings

The 17 saved rows change one factor at a time around the same reported polygon-CSF calculation. They are not 17 algorithms or jointly optimized alternative products. The reported calculation uses the 150-250 m mean wind, a 1.5 m s-1 minimum wind, a 0.30-degree background box, 20 transects, 0.70 coverage, a first transect 0.1 degree downwind, a 60-degree maximum mismatch, and low/high z = 1.7/2.4 object boundaries.

Table S5: One-factor polygon-CSF sensitivity design.

Factor	Reported calculation	Compared setting(s)	Question
Wind layer	150-250 m mean	150 m; 250 m	Does vertical wind choice change Q?
Minimum wind	1.5 m s-1	2.5 m s-1	How does stricter low-wind exclusion change calculability?
Background box	0.30 degrees	0.20; 0.40 degrees	Does local background scale change Q?
Transect count	20	15; 25	Is the event median controlled by transect count?
Transect coverage	0.70	0.50; 0.90	How does missing-pixel tolerance change inclusion?
First transect	0.1 degrees downwind	0.0; 0.2 degrees	Does the near-source start change Q?
Wind-object mismatch	no more than 60 degrees	no more than 30 degrees	How does stricter geometry change calculability?
Object boundary	low/high 1.7/2.4	low/high 2.0/2.4	Do weaker connected pixels change Q?

The reported quantitative subset contains 512 selected events with finite Q, covering 177 of 180 strict-A regions. All 512 selected events have completed the 17-setting comparison. The mutually exclusive event-level categories are 252 stable across all 17 settings, 146 stable for the reported calculation and 12 nearby settings, and 114 retaining the reported calculation without meeting either broader definition. Classifying each region by its most stable selected event is not used to define the PCA-gated reporting population; the event-level categories are reported here as sensitivity evidence. The event-Q median is 34.42 Mg h-1 (P16-P84 17.58-71.76), and the source-region median-Q median is 35.03 Mg h-1 (IQR 23.61-49.29).

S10. Output Fields and Provenance

Table S6: Core output fields and provenance.

Field	Stage	Unit	Definition
source_region_id	recurrence	identifier	Fixed-centre 25 km candidate-region identifier.
center_lat	recurrence	degrees_north	Latitude of the fixed centre established by the highest-ranked unassigned event.
center_lon	recurrence	degrees_east	Longitude of the fixed centre established by the highest-ranked unassigned event.

Continued on next page

Field	Stage	Unit	Definition
total_event_count	recurrence	events	Independent overpass-product events assigned directly within 25 km of the fixed centre; at most one event per nc_name is retained within a region.
active_year_count	recurrence	years	Number of distinct acquisition years represented by member events.
active_years	recurrence	year_list	Delimited acquisition years represented by member events.
product_role	product	category	Single-observation or recurrent candidate-region role.
recurrence_tier	recurrence	category	Exclusive total-event tier: one, 2-4, 5-9, or at least 10 events.
is_recurrent_ge2	recurrence	boolean	True when total_event_count is at least 2.
is_recurrent_ge5	recurrence	boolean	True when total_event_count is at least 5.
is_recurrent_ge10	recurrence	boolean	True when total_event_count is at least 10.
direct_score_max	pre_csf	score	Maximum saved direct pre-CSF object-usability score among member events.
direct_score_median	pre_csf	score	Median saved direct pre-CSF object-usability score among member events.
precsf_high_event_count_ge1p75	pre_csf	events	Number of member events with direct_score at least 1.75.
precsf_high_event_fraction_ge1p75	pre_csf	fraction	Fraction of member events with direct_score at least 1.75.
has_formal_facility25	facility_context	boolean	True when at least one formal catalogue record is within 25 km of an automatic-mask pixel for at least one member event.
facility_support_axis	facility_context	category	Readable Facility25 support state.
facility_supported_event_count	facility_context	events	Member events having at least one formal catalogue record within 25 km of an automatic-mask pixel.
facility_record_ids_25km	facility_context	records	Number of distinct formal catalogue record identifiers retained within 25 km across facility-supported events.

Continued on next page

Field	Stage	Unit	Definition
facility_pair_rows_25km	facility_context	event_record_pairs	Number of event-to-catalogue-record pairs satisfying the exact mask-distance threshold of 25 km.
nearest_facility_mask_distance_25km	facility_context	km	Minimum exact distance from any retained facility record to any automatic-mask pixel, restricted to Facility25 matches.
facility_names_25km	facility_context	delimited_text	Delimited names of all retained Facility25 catalogue records.
facility_catalogs_25km_complete	facility_context	delimited_text	Delimited source catalogues contributing Facility25 records.
facility_sectors_25km	facility_context	delimited_text	Delimited sectors reported by Facility25 catalogue records.
facility_statuses_25km	facility_context	delimited_text	Delimited operating-status values reported by Facility25 catalogue records.
fire_screening_axis	firms_context	category	Whether FIRMS screening is complete for the facility-supported event subset.
fire_context_axis	firms_context	category	Region-level same-day 25 km FIRMS context for facility-supported events.
nonfire25_event_count_recomputed	firms_context	events	Facility-supported events for which both FIRMS sources completed and no same-day detection matched within 25 km.
fire25_event_count_recomputed	firms_context	events	Facility-supported events with at least one same-day FIRMS detection within 25 km.
fire50_event_count_recomputed	firms_context	events	Facility-supported events with at least one same-day FIRMS detection within 50 km.

The complete data dictionary, including missing-value meanings and claim boundaries, is supplied in the machine-readable submission workbook. The table above lists the first 30 core fields needed to join event, recurrence, attribution, and quantitative outputs.

Reconstruction failure, incomplete FIRMS coverage, missing wind, low wind, insufficient background, geometric mismatch, insufficient downwind length, and insufficient transects remain explicit states. Event, source-region, sensitivity, and case tables are accompanied by run manifests and SHA-256 checksums. No failed record is silently removed to change a denominator.

S11. Navigation from Main-Text Claims to Supplementary Evidence

This section follows the main-text argument and identifies the evidence unit for each claim so that model tests, catalogue statistics, and quantitative subsets are not treated as interchangeable validation targets.

Table S7: Main-text claims and supporting supplementary evidence.

Main-text claim	Statistical unit	Key evidence	Does not establish
Weak labels support proposal ranking	Scenes and local proposals	Independent test in S7.1; proposal-propagation comparison in S8.2	Pixel truth or global industrial-source recall
Reconstructed objects can enter recurrence analysis	Observed-pixel objects	S3, S7.2, and S8.1-S8.3	That every object is a confirmed plume
ge5, ge10, and four-year support form stronger persistence tails	25 km fixed-centre regions	Opportunity denominators in S12	Random-land truth-set detection probability
Recurrence is associated with industrial facility-group context	Candidate regions and eligible events	Opportunity-adjusted models in S13	Unique-facility or causal source apportionment
Conditional Q describes instantaneous magnitude during qualified overpasses	Events and regions with reported Q	S6, S9, and S14	External accuracy, annual facility emissions, or universal independence from recurrence
Six cases connect product statistics to real facility groups	Six predefined A-tier ge10 regions	S15, Figs. 8 and 9, and main-manuscript references 22–30	High-resolution imagery validation of CO or Q

S12. Observation Opportunities, File Integrity, and Denominator Sensitivity

Crossing 13,363 catalogue locations with 20,279 physical L2 records produced 23,280,813 footprint-intersection rows and 4,792,244 opportunities under the manuscript definition. Loose/main/strict sensitivity definitions retained 8,391,996/4,792,244/3,119,473 opportunities. Eighty-seven unreadable archive paths used pre-existing integrity-checked server copies of the same products; two paths that disappeared after scanning used persisted rows from a documented successful scan of the same product; zero files remained unresolved. All 25,587 detections linked to opportunities under the manuscript definition.

Table S8: Observation-opportunity counts and detection frequencies by recurrence class.

Recurrence class	Regions	Detections	Valid opportunities	Median detection frequency	Pooled detections/ opportunities
1	8,377	8,377	2,886,653	0.0029	0.0029
2-4	4,172	10,529	1,575,449	0.0066	0.0067
5-9	646	4,036	258,598	0.0155	0.0156
at least 10	168	2,645	71,544	0.0348	0.0370

The opportunity surface was reconstructed only at catalogue source locations and does not estimate random-land recall, precision, or truth-set detection probability.

S13. Complete Product-Level Relationships Between Recurrence and Industrial Facility Groups

The recurrence-industrial relationship used two independent facility representations. The first retained the reported event objects and integrated facility catalogue to describe facility count, distance, and facility records per supported event for 5,701 Facility25 regions. The second fixed all 13,363 source-region centres and matched only Global Energy Monitor (GEM) facility entities, testing whether the principal relationship depended on event masks or the integrated catalogue. Both analyses used frozen source regions as the statistical unit and changed neither catalogue membership, evidence tier, nor Q.

S13.1. Facility-context gradients across recurrence groups

The table below is restricted to the 5,701 regions with a facility record within 25 km. Facility-name count is the deduplicated union across a region's events, and nearest distance is measured from a facility coordinate to the nearest pixel centre of a reconstructed CO object; both describe the raw product gradient. Facility records per supported event additionally remove the mechanical accumulation caused by searching facilities around a larger number of events and provide the principal facility-richness test.

Table S9: Facility-context gradients across recurrence groups.

Recurrence group	Facility25 regions	Median facility names	Median nearest-facility distance (km)	Median facility records per supported event
1 event	3,188	4.0	3.99	6.00
2-4 events	1,997	6.0	2.40	6.00
5-9 events	380	9.0	1.23	8.54
At least 10 events	136	13.5	0.55	12.27

After adding one to facility records per supported event and applying the natural logarithm, each recurrence doubling had an adjusted ratio of 1.060 (95% CI 1.034-1.086, p=4.01 x 10^{-6}; n=5,701; 463 five-degree cells). The model controlled valid observation opportunity, absolute latitude, continent, facility-catalogue density within 100 km, object quality, mean object area, and elongation. The result supports richer candidate-facility context around each retained event as recurrence increases, rather than only more repeated facility searches within a region.

S13.2. Fixed-centre GEM facility and sector sensitivity

GEM names were standardized, and same-name records within 5 km were merged as one facility entity. Across all 13,363 frozen source-region centres, the adjusted odds ratios per recurrence doubling for the presence of a GEM facility within 25, 50, and 100 km were 1.53, 1.38, and 1.15. The 25-km radius is the main facility-presence test. The decreasing effect with increasing radius is consistent with nearby industrial context being more discriminating than broad catalogue background.

Table S10: Adjusted association between recurrence and nearby GEM facilities by radius.

Fixed-centre radius	Adjusted OR per recurrence doubling	95% CI	Statistical unit
25 km	1.53	1.42-1.64	13,363 source regions
50 km	1.38	1.27-1.50	13,363 source regions
100 km	1.15	1.05-1.25	13,363 source regions

Facility-presence models controlled valid observation opportunity, absolute latitude, continent, and object quality and geometry; facility-catalogue density within 100 km was not included in these fixed-centre models. Standard errors were clustered across 613 five-degree spatial cells. This sensitivity is independent of event masks and the integrated catalogue, but it still describes association with known industrial context rather than a unique emitting facility.

The fixed-centre 50-km sector analysis showed the strongest recurrence relationship for iron and steel. The shares below are the proportions of all source regions with the corresponding

GEM sector context; sectors overlap and are not exclusive source fractions. All four recurrence coefficients had Benjamini-Hochberg $q<0.001$ within the radius.

Table S11: GEM sector context across recurrence groups and adjusted associations.

GEM sector context	One-event share	At-least-ten-event share	Adjusted OR per recurrence doubling	95% CI
Iron and steel	5.7%	34.5%	1.80	1.64-1.98
Oil and gas	12.7%	40.5%	1.52	1.41-1.65
Combustion and power	23.2%	64.3%	1.50	1.39-1.61
Cement	11.7%	39.9%	1.49	1.38-1.61

S13.3. Tier-A facility groups and country-sector combinations

Sector labels for the 180 tier-A regions remain multi-label and non-exclusive. Combustion and power, cement, oil and gas, iron and steel, and coal-mining context occurred in 170, 123, 122, 94, and 65 regions. The mutually exclusive facility-group summary classified 136 regions as mixed industrial facility groups, 37 as generic industrial contexts, and seven as single-dominant sectors. The classification used event support and distance weights and did not use Q.

Table S12: Tier-A region counts for leading country-sector combinations.

Country	Tier-A regions	Combustion and power	Cement	Oil and gas	Iron and steel	Coal mining
China	63	63	44	38	53	41
Iran	18	17	17	17	10	0
Kazakhstan	13	13	8	11	8	6
United States	13	9	3	10	6	2

These values describe source-region sector context under the frozen discovery chain and current facility catalogues. They are not national emission totals, production rankings, or sectoral emission fractions.

S14. Q Relationships, Within-Region Variation, and External Magnitude Anchors

Across the 177 regions with reported Q, raw recurrence count versus region-median Q had Spearman rho=-0.018 (95% bootstrap CI -0.157 to 0.122), and opportunity-normalized detection frequency versus Q had rho=-0.049 (-0.185 to 0.096). After applying ln(Q) and controlling facility count, sector richness, nearest-facility distance, valid observation opportunity, facility-catalogue density within 100 km, latitude, continent, and object quality and geometry, the Q ratio per recurrence doubling was 1.017 (95% CI 0.91-1.14). None of the three analyses supports substituting recurrence for instantaneous Q during qualified overpasses.

The common population for within-region variation comprised 173 regions with at least two reported Q values. The median maximum-to-minimum ratio was 2.26, and 100 regions (57.8%) exceeded a ratio of two. This result describes the range of conditional Q among retained overpasses. It cannot separate winds, background, and object geometry from true emission changes and is therefore not interpreted as operational variability or measurement error.

The main text uses only two pre-verified city-scale cross-study magnitude anchors. Both region-median Q values from this study fall within the corresponding literature intervals.

Table S13: Cross-study city-scale emission-rate magnitude anchors.

Region	This-study region-median Q (Mg h^{-1})	Published city-scale Q (Mg h^{-1})	Published interval (Mg h^{-1})	Source
Lahore	28.323	31.735	20.548-43.607	Leguijt et al. (2026) doi:10.1029/2025JD044636
Khartoum	41.009	45.205	38.356-49.315	Leguijt et al. (2023) doi:10.5194/acp-23-8899-2023

The comparisons use the same satellite and a related CSF method family, but city footprints and overpass samples differ. They support case-level cross-study magnitude consistency, not same-event, independent-instrument, or product-wide absolute-accuracy validation.

S15. Summary of the Six Dual-Scale Cases

Table S14: Summary of the six dual-scale industrial cases.

Case	Region	Real-world facility group	Recurrence	Reported-Q events	Illustrated Q (Mg h^{-1})
01	r25_00546	Jiugang steel and captive power	20	3	28.3
02	r25_00093	Esfahan integrated steel	25	3	43.1
03	r25_00330	Guotai coal chemistry and captive power	13	3	56.2
07	r25_00066	Magnitogorsk steel and CHP	19	2	49.5
16	r25_00639	Karaganda coal CHP	11	3	46.6
19	r25_02871	Mashhad gas-fired power	12	3	23.6

Each plate contains the TROPOMI object and reported polygon-CSF geometry, the complete mask on regional Esri imagery, and an independent facility close-up. Imagery provides facility-group and land-use context only; dates may differ, and it validates neither Q, CO, nor unique-facility causality.

S16. Scope of Supported Claims

The evidence supports weak-label scene ranking, deterministic corrected-CO objects, recurrent TROPOMI-scale candidate regions, facility and same-day active-fire context, and conditional instantaneous fluxes for events meeting the declared geometric and meteorological conditions.

It does not support global plume recall, pixel-level segmentation accuracy, confirmed point sources, unique facility attribution, externally validated absolute Q accuracy, or annual emission inventories. The candidate product, evidence tiers, CSF-input population, successful event estimates, and selected quantitative records use different denominators and must not be collapsed into one confidence score.

References

[5] Borsdorff, T. et al. Improving the TROPOMI CO data product: update of the spectroscopic database and destriping of single orbits. Atmospheric Measurement Techniques 12, 5443-5455 (2019). https://doi.org/10.5194/amt-12-5443-2019

[13] Schroeder, W., Oliva, P., Giglio, L. & Csiszar, I. A. The new VIIRS 375 m active fire detection data product: Algorithm description and initial assessment. Remote Sensing of Environment 143, 85-96 (2014). https://doi.org/10.1016/j.rse.2013.12.008

[14] Hersbach, H. et al. The ERA5 global reanalysis. Quarterly Journal of the Royal Meteorological Society 146, 1999-2049 (2020). https://doi.org/10.1002/qj.3803